NET-Triggered NLRP3 Activation and IL18 Release Drive Oxaliplatin-Induced Peripheral Neuropathy

Tongtong Lin[1], Liang Hu[1], Fan Hu[1], Kun Li[1], Chao-Yu Wang[1], Li-Juan Zong[1], Ya-Qian Zhao[1], Xiaotao Zhang[2], Yan Li[3], Yang Yang[4], Yu Wang[1], Chun-Yi Jiang[1], Xuefeng Wu[5], and Wen-Tao Liu[1]

ABSTRACT

Oxaliplatin is an antineoplastic agent frequently used in the treatment of gastrointestinal tumors. However, it causes dose-limiting sensorimotor neuropathy, referred to as oxaliplatin-induced peripheral neuropathy (OIPN), for which there is no effective treatment. Here, we report that the elevation of neutrophil extracellular traps (NET) is a pathologic change common to both cancer patients treated with oxaliplatin and a murine model of OIPN. Mechanistically, we found that NETs trigger NLR family pyrin domain containing 3 (NLRP3) inflammasome activation and the subsequent release of IL18 by macrophages, resulting in mechanical hyperalgesia. In NLRP3-deficient mice, the mechanical hyperalgesia characteristic of OIPN in our model was reduced. In addition, in the murine model, treatment with the IL18 decoy receptor IL18BP prevented the development of OIPN. We further showed that eicosapentaenoic acid (EPA) reduced NET formation by suppressing the LPS–TLR4–JNK pathway and thereby abolished NLRP3 inflammasome activation and the subsequent secretion of IL18, which markedly prevented oxaliplatin-induced mechanical hyperalgesia in mice. These results identify a role for NET-triggered NLRP3 activation and IL18 release in the development of OIPN and suggest that utilizing IL18BP and EPA could be effective treatments for OIPN.

Introduction

Oxaliplatin is a platinum-derivative chemotherapeutic agent used in to treat patients with digestive tumors in the adjuvant and metastatic settings (1). Neurotoxicity is the most severe adverse effect of oxaliplatin. Oxaliplatin-induced peripheral neuropathy (OIPN) is thus a serious dose-limiting side effect contributing to significant loss of functional abilities, negatively impacting quality of life, and ultimately affecting overall survival rates (2–4). At present, no therapeutic strategies are effective in the treatment of OIPN.

The complex mechanisms underlying OIPN pathogenesis are not fully understood. Based on studies in rodent models of OIPN, several factors, such as neuroinflammation, mitochondrial damage, oxidative stress, ion channel changes, and degeneration of peripheral nerves,

have been proposed as determinants of OIPN pathogenesis (3, 5, 6). Among the players in neuropathic pain, inflammation has been indicated as a potential common driver of OIPN. Oxaliplatin induces a striking upregulation of inflammatory genes in dorsal root ganglia (DRG) and a release of proinflammatory cytokines and chemokines from macrophages, including IL1β, IL6, and TNFα (7, 8). However, the signaling pathways leading to cytokine release, as well as the contributions of these to the development of oxaliplatin-induced mechanical hyperalgesia, are not fully understood.

One group has reported that gut microbes can promote the development of chemotherapy-induced mechanical hyperalgesia (9). They show that oxaliplatin increases gut microbe–derived lipopolysaccharide (LPS) in the serum and DRG, and that this stimulates the inflammatory response. In this study, we demonstrate that gut microbe–derived LPS triggers the formation of NETs during OIPN. NETs are extracellular strands of decondensed DNA in complex with histones and granule proteins that are expelled from dying neutrophils to ensnare and kill microbes (10). In the process of NET formation, neutrophil elastase (NE) and myeloperoxidase (MPO) contribute to nuclear membrane permeabilization and further unfolding of chromatin. Peptidyl arginine deiminase 4 (PAD4) is a Ca^{2+}-specific enzyme primarily localized in the nucleus that is indispensable for the generation of NETs (11, 12).

NETs have been associated with autoimmune disorders, cardiovascular and pulmonary diseases, inflammation, and thrombosis (13). In atherosclerosis, cholesterol crystals trigger neutrophils to release NETs, and then NETs activate the NLR family pyrin domain containing 3 (NLRP3) inflammasome, leading to IL1β release (14). Starobova and colleagues reported that vincristine-induced peripheral neuropathy is driven by canonical NLRP3 activation and IL1β release (15). However, the mechanisms by which vincristine induces the activation of NLRP3 are unknown. Taken together, we hypothesized that NETs may play a critical role in the pathogenesis of OIPN by upregulating cytokines.

Here, we demonstrate that oxaliplatin elicits the release of IL18 and IL1β in humans and mice and that this is driven by NET-triggering of NLRP3 activation via the TLR7/TLR9 signaling pathway. OIPN did

[1]Jiangsu Key Laboratory of Neurodegeneration, Department of Pharmacology, Nanjing Medical University, Nanjing, Jiangsu, China. [2]Department of Radiation Oncology, Qingdao Central Hospital, Qingdao, Shandong, China. [3]Department of Oncology, Shandong Provincial Qianfoshan Hospital, The First Hospital Affiliated with Shandong First Medical University, Jinan, Shandong, China. [4]The Affiliated Cancer Hospital of Nanjing Medical University, Jiangsu Cancer Hospital, Jiangsu Institute of Cancer Research, Nanjing, Jiangsu, China. [5]State Key Laboratory of Pharmaceutical Biotechnology, School of Life Sciences, Nanjing University, Nanjing, Jiangsu, China.

T. Lin, L. Hu, and F. Hu contributed equally to this work.

Corresponding Authors: Chun-Yi Jiang, Department of Pharmacology, Nanjing Medical University, 101 Longmian Avenue, Jiangning District, Nanjing, 211166, Jiangsu Province, China. Phone: 025-8686-9338; E-mail: jcy@njmu.edu.cn; Xuefeng Wu, 22 Hankou Road, Gulou District, Nanjing, 210093, Jiangsu Province, China. Phone: 025-8968-1312; E-mail: wuxf@nju.edu.cn; and Wen-Tao Liu, 101 Longmian Avenue, Jiangning District, Nanjing, 211166, Jiangsu Province, China. Phone: 025-8686-9338; E-mail: painresearch@njmu.edu.cn

not develop in Nlrp3$^{-/-}$ mice. Moreover, the utilization of the IL18 decoy receptor IL18BP prevented the development of oxaliplatin-induced mechanical hyperalgesia; however, the IL1R antagonist anakinra did not improve oxaliplatin-induced mechanical hyperalgesia. IL18-induced phosphorylation of GluN2B Tyr1472 was shown to be the key determinant of OIPN pathogenesis.

Finally, we found that eicosapentaenoic acid (EPA) effectively suppressed NET formation by inhibiting the LPS–TLR4–JNK pathway and abolished NLRP3 inflammasome activation and the subsequent secretion of IL18, which markedly prevented oxaliplatin-induced mechanical hyperalgesia in mice. These results suggest that treatment with IL18BP and/or EPA could be a viable clinical strategy to prevent the development of OIPN.

Materials and Methods

Patients and clinical data

This study was conducted in accordance with the Council for International Organizations of Medical Sciences International Ethical Guidelines for Biomedical Research Involving Human Subjects. The procedures were performed according to a protocol approved by the Ethics Committee of the First Affiliated Hospital of Nanjing Medical University (Nanjing, China; 2021-SR-571). Written informed consent was obtained from all participants.

Samples of peripheral blood were obtained from 20 patients at the First Affiliated Hospital of Nanjing Medical University (Nanjing, China), and all methods were carried out in accordance with relevant guidelines and regulations. A total of 20 patients, 10 who had received chemotherapy and 10 who had not, and 10 healthy adult volunteers were enrolled in the study. For the patients who had not received chemotherapy, the blood samples were collected at the time they were diagnosed with cancer for the patients who received chemotherapy, the blood samples were collected at the time they began to receive neurotoxic chemotherapy and then they developed new numbness, tingling, and/or pain in their hands and/or feet. The plasma was separated by centrifugation and then frozen at $-80°C$ for all experiments.

The baseline characteristics of the patients with cancer who had not received chemotherapy are summarized in Supplementary Table S1. The median age of the patients was 70 (range, 50–82), and 40% of patients were female. The baseline characteristics of the patients with cancer who had been treated with chemotherapy are summarized in Supplementary Table S2. The median age of the patients was 71 (range, 53–76), and 50% of patients were female. The inclusion criteria were as follows: (i) Karnofsky score > 50%; (ii) expected survival time > 3 months; (iii) at least one measurable lesion confirmed by CT or PET-CT; (iv) normal bone marrow reserve and heart, liver, and kidney function; (v) no serious complications and no second primary tumors; and (vi) oxaliplatin or oxaliplatin combination therapy. (vii) All patients had different degrees of functional impairment (difficulty grasping, walking, wearing clothes, and inability to wear closed shoes). Pain intensity was measured by the visual analog scale (VAS). VAS is most commonly a straight 100-mm line, without demarcation, that has the words "no pain" at the leftmost end and "worst pain imaginable" (or something similar) at the rightmost end. Patients are instructed to place a mark on the line indicating the amount of pain that they feel at the time of the evaluation. The distance of this mark from the left end is then measured, and this number is used as a numeric representation of the severity of the patient's pain.

Animals and the OIPN model

All procedures were performed in strict accordance with the regulations of the ethics committee of the International Association for the Study of Pain and the Guide for the Care and Use of Laboratory Animals (The Ministry of Science and Technology of China, 2006). All animal experiments were approved by the Nanjing Medical University Animal Care and Use Committee (No. IACUC-1903031 and No. IACUC-2005001) and were designed to minimize suffering and the number of animals used.

All animals used in experiments were male. Adult C57BL/6J mice (20–25 g wild-type) were purchased from the Animal Core Facility of Nanjing Medical University, Nanjing, China. Pad4$^{-/-}$ mice were purchased from Jackson Laboratory (030315). Nlrp3$^{-/-}$ mice were obtained from Shuo Yang (Nanjing Medical University). Animals were housed five to six per cage under pathogen-free conditions with soft bedding under controlled temperature (22°C ± 2°C) and photoperiods (12:12-hour light–dark cycle). The animals were habituated to these conditions for at least 2 days before starting experiments. Animals were randomly divided into groups. The sample size was designed on prior experience and to be limited to the minimal as scientifically justified. For each group of experiments, the animals were matched by age and body weight. Intraperitoneal injections of oxaliplatin (3 mg/kg; H20093168, Qilu Pharmaceutical Co. Ltd) or saline were conducted from days 1 to 5 to establish the animal model of OIPN. Doses of oxaliplatin were based on previous studies using well-validated murine models of OIPN (9). Mechanical sensitivity was detected by the von Frey test before oxaliplatin administration every morning (16). In brief, animals were placed in boxes set on an elevated metal mesh floor and allowed 30 minutes for habituation before testing. The plantar surface of each hind paw was stimulated with a series of von Frey Filaments with logarithmically incremental stiffness perpendicular to the plantar surface. Each mouse was tested 3 times, and the average of the threshold was measured. Threshold is a measure of when the animal becomes aware of the presence of a mechanical stimulus that causes irritation. Behavioral tests were performed blindly.

Drug treatment

For the assessment of chemotherapeutics other than oxaliplatin, mice were intraperitoneally injected with carboplatin (CBP; 10 mg/kg) 3 times (days 1, 3, and 7); cisplatin (DDP; 2.3 mg/kg) for 5 consecutive days; paclitaxel (PTX; 8 mg/kg) 3 times (day 1, 3, and 5); and vincristine (VLB; 100 μg/kg) for 5 consecutive days to induce mechanical hyperalgesia.

For the assessment of mechanical hyperalgesia, mice were administered the protein arginine deiminase 4 (PAD4) inhibitor Cl-amidine (S8141, Selleck; 10 mg/kg, i.p.), the myeloperoxidase (MPO) inhibitor PF-1355 (HY-100873, MedChemExpress; 50 mg/kg, i.p.), the NLRP3 inhibitor MCC950 (S8930, Selleck; 20 mg/kg, i.p.), the TLR7 and TLR9 inhibitor IRS954 (1 mg/kg, i.p.), anakinra (HY-108841, MedChemExpress; 2.5 mg/kg, i.p.), IL18BP (Z03168, GenScript; 200 μg/kg, i.p.) or saline 1 day before oxaliplatin administered once a day until the end of 14 days. IRS954 sequence, 5'-TGCTCCTGGAGGGGTTGT-3'.

For neutrophil depletion, mice were administered 300 μg anti-mouse Ly6G (1A8 clone; specific for neutrophils, BE0075-1, Bio X Cell) 1 day before the initiation of oxaliplatin treatment to the 14th day every 3 days. For gut microbiota eradication, mice were provided with drinking water containing 0.5 g/L ampicillin, 0.5 g/L neomycin, 0.5 g/L metronidazole, and 0.25 g/L vancomycin (HY-B0522, HY-B0470, HY-B0318, and HY-B0671, MedChemExpress) with 3 g/L artificial sweetener Splenda (HY-N0614, MedChemExpress) for 3 weeks. Antibiotic

water was maintained during the entire experimental period for oxaliplatin-induced pain.

To validate that the components DNA and RNA of NETs contribute to the development of OIPN, mice were injected with DNase1 (D5025, Sigma; 150 U, i.v.) from the first day of modeling to the 14th day or from the sixth day of modeling to the 14th day. Mice were injected with RNase1 (DNase, protease-free, Thermo Fisher, EN0531; 1 mg/kg, i.v.) from the first day of modeling to the 14th day or from the sixth day of modeling to the 14th day.

To verify the ability of IL18BP to inhibit IL18 signaling *in vivo*, recombinant mouse IL18 (HY-P73181, MedChemExpress; 20 ng per mouse, i.p.) was administered to $Nlrp3^{-/-}$ mice for 7 consecutive days. To investigate the role IFNγ in OIPN, mice were administered 100 μg anti-mouse IFNγ (BE0055-1, Bio X Cell, NH) 1 day before the initiation of oxaliplatin treatment until the end of 14 days. Mice were treated with EPA (HY-B0660, MedChemExpress; 1 g/kg, i.g.) 5 days before oxaliplatin administration until the end of 14 days.

Quantification of NETs

Mouse plasma and human plasma were collected from whole blood by centrifugation at 3,000 rpm for 5 minutes. NETs in plasma were quantified according to the manufacturer's instructions with the Citrullinated Histone H3 ELISA Kit (501620, Cayman), NETosis Assay Kit (601010, Cayman), and Quant-iT PicoGreen dsDNA Assay kit (P11496, Invitrogen). The absorbance was measured by a microplate reader (Multiskan FC, Thermo Fisher).

LPS (endotoxin) assay

All materials used for both sample preparation and testing were pyrogen free. LPS concentrations in plasma and tissue homogenate from mice were measured by an endotoxin assay based on a limulus amebocyte extract with a chromogenic limulus amebocyte lysate (LAL) assay (Pierce LAL Chromogenic Endotoxin Quantitation Kit, A39553, Thermo Scientific). Samples were diluted in pyrogen-free water and heated to 70°C for 10 minutes to inactivate inhibitor agents that could interfere with the assay. All samples were tested in triplicate. The absorbance was measured by a microplate reader (Multiskan FC). The endotoxin content was expressed as endotoxin units per milliliter (EU/mL).

Bacteria culture test

We tested for the presence of bacteria in blood samples from oxaliplatin-treated mice. The samples of mouse blood were collected after 12 and 24 hours of oxaliplatin administration, and then 10 μL mouse blood was inoculated into LB solid medium and LB liquid medium at 37°C for 24 hours.

ELISA

Levels of IL1β, IL6, and TNFα in mouse plasma and DRG were evaluated by ELISA kits (MLB00C, M6000B, and MTA00B, R&D Biosystems). Levels of IL18 in mouse plasma and human plasma were measured by ELISA kits (MM-0169M1 and MM-0139H2, Mmbio). All ELISAs were performed according to the manufacturer's instructions.

MPO activity assay

Mouse DRG were homogenized in 50 mmol/L potassium phosphate buffer, centrifuged, and suspended in 0.5% cetytrimethyl ammonium bromide in potassium phosphate buffer. The suspensions were sonicated for 30 s with 3 freeze–thaw cycles in liquid nitrogen. After centrifugation, 40 μL of supernatant was incubated with 100 μL

tetramethylbenzidine solution, and the reaction was stopped with 100 μL 2 N HCl. The optical density was measured at 450 nm by Cytation 5 cell imaging multimode reader (BioTek).

Immunofluorescence microscopy of murine DRG, spinal cord, and cells

DRG tissues and spinal cord tissues. After deep anesthesia by i.p. injection of 1% pentobarbital sodium (100 mg/kg, i.p.), mice were perfused transcardially with normal saline followed by 4% paraformaldehyde in 0.1 M PB, pH 7.4, each for 20 minutes. Then, lumbar 5 DRGs and lumbar 4–5 spinal cord were dissected out and postfixed in 4% paraformaldehyde for 24 hours and cryoprotected overnight in 30% sucrose. The embedded blocks were sectioned as 10 μm thick. Blocking was achieved using 1% normal donkey serum (017-000-121, Jackson ImmunoResearch) and 0.1% Triton X in PBS for 1 hour. DRG specimens were incubated with anti-F4/80 (ab6640, Abcam), anti-Ly6G (127636, BioLegend), and anti-H3Cit (ab5103, Abcam) overnight at 4°C. Spinal cord specimens were incubated with anti-c-fos (2250S, Cell Signaling Technology) and CGRP (14959, Cell Signaling Technology). The secondary antibodies used were as follows: Alexa Fluor 594–conjugated donkey anti-mouse (715-585-150, Jackson ImmunoResearch) and Alexa Fluor 488-conjugated donkey anti-rat (712-025-150, Jackson ImmunoResearch), for 2 hours at room temperature. After washing 3 times with PBS, the samples were studied under a fluorescence microscopy (LEICA DM2500) for morphologic details of the immunofluorescence staining. Examination was carried out blind.

In vitro NET assay. For immunofluorescence staining, freshly isolated polymorphonuclear neutrophils (PMNs) from the bone marrow (isolated as described in "Neutrophil isolation") were seeded on poly-D-lysine-coated coverslips and allowed to adhere. Cells were treated with LPS (1 μg/mL, L2880, Sigma-Aldrich), oxaliplatin (10 μmol/L), or oxaliplatin (10 μmol/L) + LPS (10 ng/mL). Cells were fixed for 15 minutes with 4% paraformaldehyde (PFA) and blocked with 1% BSA and 0.3% Triton X-100 in PBS for 30 minutes. Then, rabbit anti-H3Cit and mouse anti-MPO (ab90810, Abcam) primary antibodies were used overnight at 4°C. After three washes, donkey anti-rabbit Alexa Fluor 488 (A-21207, Invitrogen) and donkey anti-mouse Alexa Fluor Cy3 (715-585-150, Jackson ImmunoResearch) were added for 2 hours at room temperature. NET formation was visualized by fluorescence microscopy (LEICA DM2500).

Extracellular DNA and RNA of NETs. PMNs from the bone marrow (isolated as described in *Neutrophil isolation*) were incubated with LPS (1 μg/mL) for 4 hours. RNase A (100 μg/mL, EN0531, Thermo Fisher) and DNase 1 (10 U/mL, D5025, Thermo Fisher) were administered for 1 hour after LPS treatment. Then, the cells were fixed with 4% PFA and stained with 1 μmol/L Sytox Green (S7020, Thermo Fisher) or 50 μmol/L Syto RNAselect Green (S32703, Thermo Fisher) for 15 minutes. Images were captured using fluorescence microscopy (LEICA DM2500).

Macrophage endocytosis of NETs. NETs (isolated as described in "NET isolation") were incubated with bone marrow–derived macrophages (BMDM; see "BMDM isolation") for 1 hour in DMEM (KGM12800N-500, Keygen Biotech) culture medium supplemented with 10% FBS. Then, BMDMs were fixed for 15 minutes with 4% PFA and blocked with 1% BSA and 0.3% Triton X-100 in PBS for 30 minutes. Then, rabbit anti-H3Cit, mouse anti-TLR7 (NBP2-27332, Novus Biologicals), or mouse anti-TLR9 (ab134368, Abcam) primary antibodies were used overnight at 4°C. After three washes, donkey anti-rabbit Alexa Fluor 488 (A-21207, Invitrogen) and donkey anti-mouse Alexa Fluor 594 (715-585-150, Jackson ImmunoResearch) were

added for 2 hours at room temperature. Then, the samples were observed by confocal microscopy (Zeiss LSM 800).

NETs were stained with Sytox Orange (1 µmol/L, S34861, Thermo Fisher) for 30 minutes and then incubated with BMDMs for 1 hour. Then, the BMDMs were fixed for 15 minutes with 4% PFA and blocked with 1% BSA and 0.3% Triton X-100 in PBS for 30 minutes. Then, rabbit anti-TLR7 (A0091, Abclonal) or rabbit anti-TLR9 (TD2970s, Abmart) primary antibodies were used overnight at 4°C. After three washes, donkey anti-rabbit Alexa Fluor 488 (A-21207, Invitrogen) was added for 2 hours at room temperature. Then, the samples were observed by confocal microscopy (Zeiss LSM 800).

Neutrophil isolation

Neutrophil isolation was performed based on a previously described method (17). In brief, after mice were euthanized and sprayed with 75% ethanol, the femur and tibia were extracted. A 25-gauge needle and a 10-cc syringe filled with RPMI-1640 (KGM31800N-500, Keygen Biotech) supplemented with 10% FBS (04-001-1ACS, Biological Industries) and 2 mmol/L EDTA (E9884, Sigma-Aldrich) was used to flush the bone marrow cells from both ends of the bone shafts into a 50-mL centrifuge tube. The cells were centrifuged at $1,200 \times g$ for 5 minutes at 4°C, resuspended in 3 mL sodium chloride physiologic solution, and then layered on top of 9 mL Histopaque 1077 (density, 1.077 g/mL, 10771, Sigma-Aldrich) in a 50-mL conical tube. After centrifugation for 20 minutes at $2,000 \times g$ without braking, the supernatant was discarded, and the cells were resuspended in 5 mL sodium chloride physiologic solution. The cells were then layered on top of 10 mL of Histopaque 1119 (density, 1.119 g/mL, 11191, Sigma-Aldrich) in a 50-mL conical tube and centrifuged for 20 minutes at $2,000 \times g$ without braking. Neutrophils were collected at the interface of the Histopaque 1119 and sodium chloride physiologic solution. The collected neutrophils were washed with RPMI-1640 supplemented with 10% FBS and 1% penicillin/streptomycin (KGY0023, Keygen Biotech) for twice and centrifuged at 1,400 rpm for 7 minutes at 4°C.

To assess the inhibition of EPA or DHA on NET formation, neutrophils were incubated with LPS (1 µg/mL) for 4 hours. DHA (20 µmol/L, HY-B2167, MedChemExpress) or EPA (20 µmol/L, HY-B0660, MedChemExpress) was added to the medium 1 hour before LPS. Then, the cells were stained with 1 µmol/L Sytox Green (S7020, Thermo Fisher) for 15 minutes, and fluorescence intensity was captured at an emission peak of 523 nm when excited by a 488 nm argon-ion laser (Cytation 5, BioTek).

NET isolation

NET isolation was performed as previously described (18). Neutrophils, isolated as described in "Neutrophil isolation," were stimulated with LPS (1 µg/mL) for 4 hours in RPMI-1640 supplemented with 10% FBS and 1% penicillin/streptomycin. After stimulation, the supernatant was discarded, leaving NETs and neutrophils adhered at the bottom of the petri dish. 15 mL cold PBS (without Ca^{2+} and Mg^{2+}) was used to lift off all adherent NETs and neutrophils from the bottom. After centrifugation for 10 minutes at $450 \times g$ at 4°C, neutrophils were in the pellet at the bottom and cell-free NETs were in the supernatant. The supernatant was divided into 1.5 mL microcentrifuge tubes and centrifuged for 10 minutes at $18,000 \times g$ at 4°C. This step allowed NETs to precipitate to the bottom. The supernatant was discarded and the pellets were resuspended in cold PBS. The NET concentration in the sample was measured by NanoDrop spectrophotometer. The adequate concentration in the sample for further assays should range between 140 and 180 ng/µL.

BMDM isolation

BMDM cells were harvested from the femurs and tibia of C57BL6/J mice. The culture medium used to differentiate and maintain BMDM cells was DMEM supplemented with 10% (v/v) FBS, 1% penicillin/streptomycin, and 10% L929 cell supernatant. BMDMs were seeded in 6-well tissue culture plates at day 7. To identify which TLR was critical in NET-triggered cytokine production, we pretreated BMDMs with inhibitors of TLR2 (C29, HY-100461, MedChemExpress), TLR4 (TAK242, HY-11109, MedChemExpress), TLR7 (IRS661, Genepharma), TLR8 (CU-CPT9a, HY-11266, MedChemExpress), or TLR9 (IRS869, Genepharma) for 1 hour and then stimulated them with NETs (500 ng/mL) for 3 hours. The levels of *Il1b*, *Il6*, and *Tnfa* mRNA were measured by quantitative real-time PCR analysis ($n = 3$; see "Quantitative real-time PCR analysis"). IRS661 sequence: 5'-TGCT-TGCAAGCTTGCAAGCA-3'. IRS869 sequence: 5'-TCCTGGAGGG-GTTGT-3'.

Western blot

Samples (cells or DRG tissue) were collected and washed with ice-cold PBS before being lysed in lysis buffer (P0013B, Beyotime Biotechnology). Sample lysates were separated by SDS–PAGE and electrophoretically transferred onto polyvinylidene fluoride membranes. The membranes were blocked with 10% whole milk in TBST (Tris–HCl, NaCl, Tween 20) for 2 hours at room temperature and probed with primary antibody at 4°C overnight. The primary antibodies used were specific for citrullinated histone H3 (H3Cit; ab5103, Abcam), H3 (A2348, Abclonal), IL1β (AF-401-NA, R&D Systems), NLRP3 (AG-20B-0042-C100, Adipogen), caspase-1 (p20; AG-20B-0014-C100, Adipogen), phospho-SAPK/JNK (Thr183/Tyr185; 9255s, Cell Signaling Technology), NF-κB p65 (D14E12, Cell Signaling Technology), phospho-NF-κB p65 (S536; AP0475, Abclonal), phospho-GluN2B (Tyr1472; 4208s, Cell Signaling Technology), GluN2B (A11643, Abclonal), IFNγ (A12450, Abclonal), and β-actin (A5441, Sigma). Then, the membranes were incubated with horseradish peroxidase (HRP)–coupled secondary antibodies from Sigma. The following secondary antibodies were used: HRP-conjugated affinipure goat anti-rabbit IgG (H + L; AP307P, Sigma-Aldrich), HRP-conjugated affinipure goat anti-mouse IgG(H + L; AP308P, Sigma-Aldrich), and HRP-conjugated affinipure donkey anti-goat IgG (H + L; AP180P, Sigma-Aldrich). Data were acquired with a molecular imager chemidocxrs system (ChemiDoc XRS+, Bio-Rad), and analyzed with ImageJ (1.51 version, Rawak Software).

Quantitative real-time PCR analysis

Total RNA was extracted from BMDMs or DRGs using TRIzol reagent (15596018, Invitrogen). Isolated RNA was reverse-transcribed into cDNA using HiScript II Q RT SuperMix for qPCR (R222-01, Vazyme Biotech Co., Ltd) following a standard protocol. Quantitative real-time PCR (qPCR) was performed with ChamQ SYBR qPCR Master Mix (Q711-02, Vazyme Biotech Co., Ltd) with a QuantStudio 5 Real-Time PCR Detection System (Thermo Fisher Scientific). The relative expression levels of *Tnfa*, *Il1b*, *Il6, Arg1, Fizz1, Inos,* and *Cd206* were calculated and quantified with the $2-\Delta\Delta Ct$ method after normalization with reference. All primers used are listed in Supplementary Table S3.

siRNA knockdown

Mouse *Nlrp1*-, *Aim2*-, *Nlrp3*-, *Nlrc4*-, and *Arrb2*-targeting siRNAs were obtained from Santa Cruz Biotechnology (sc-63287, sc-140968, sc-45470, sc-60329, sc-29743, respectively). BMDM cells were
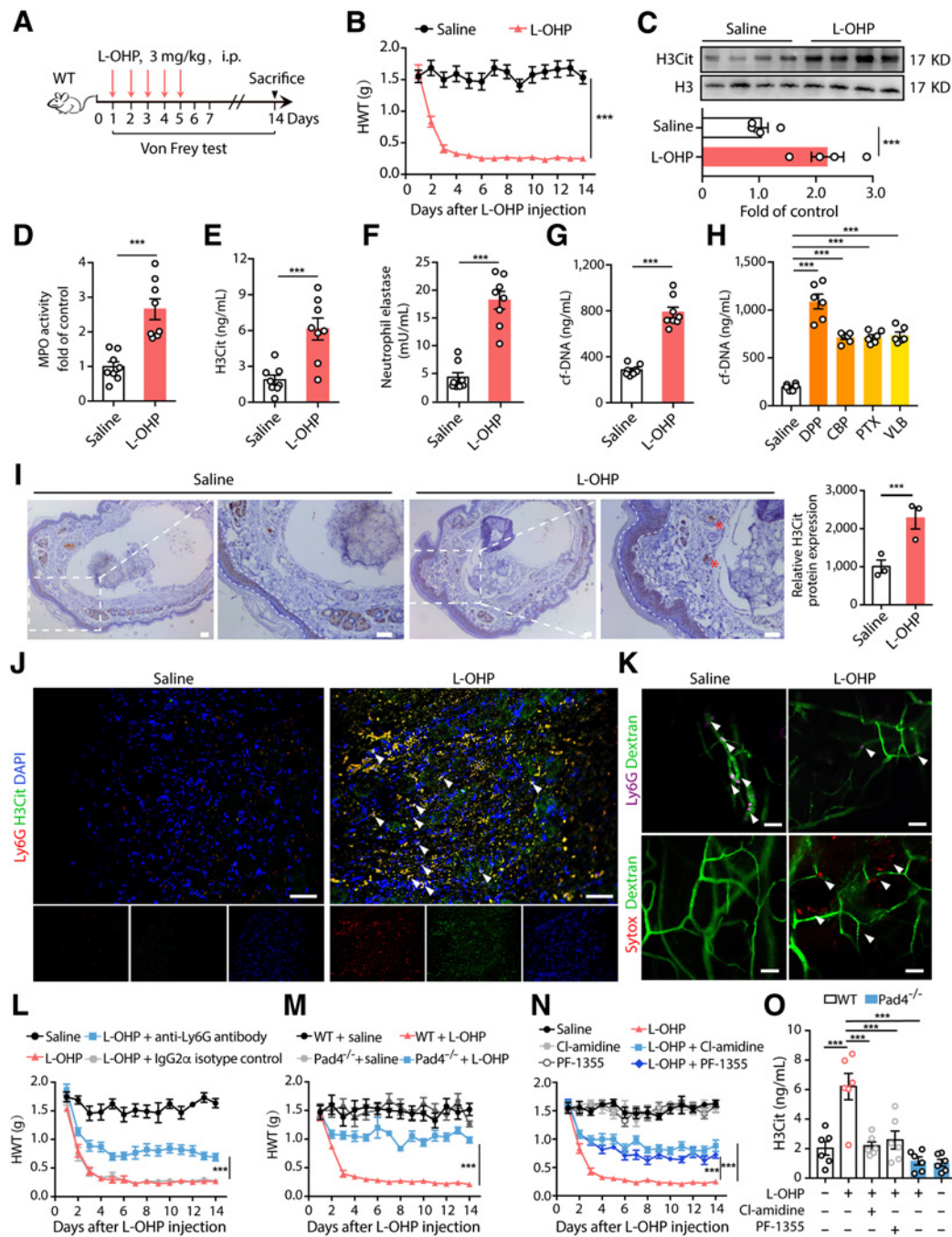
Figure 1.

Chemotherapy triggers NET formation. **A** and **B,** Adult male C57BL/6J mice were intraperitoneally injected with L-OHP (3 mg/kg) for 5 consecutive days for a total dose of 15 mg/kg to induce mechanical hyperalgesia. The mechanical pain threshold was tested for 14 days by the von Frey test ($n = 8$). L-OHP = oxaliplatin. **C,** The protein level of H3Cit in the DRG was evaluated by western blot on the 14th day after the initiation of L-OHP treatment ($n = 4$). **D,** Quantification of MPO activity was assessed in the DRG on day 14 after the initiation of L-OHP treatment ($n = 8$). **E–G,** The content of H3Cit, NE, and cfDNA in plasma after intraperitoneal injection of L-OHP was evaluated using the H3Cit ELISA kit, NETosis Assay, and Quant-iTPico green dsDNA assay, respectively, at day 14 after the initiation of L-OHP treatment ($n = 8$). **H,** Mice were intraperitoneally injected with carboplatin (CBP; 10 mg/kg) three times (days 1, 3, and 7); cisplatin (DDP; 2.3 mg/kg) for 5 consecutive days; paclitaxel (PTX; 8 mg/kg) three times (days 1, 3, and 5); and vincristine (VLB; 100 µg/kg) for 5 consecutive days to induce mechanical hyperalgesia. Then, the level of cf-NDA in plasma was evaluated by Quant-iTPico green dsDNA assay at day 7 after the initiation of chemotherapeutic drugs ($n = 6$). **I,** Representative IHC images of hind paw cross-sections stained with the NET marker H3Cit from mice treated with saline or L-OHP. The zones of the dermis and subcutaneous tissue are labeled with dotted lines, and the arteries are labeled with asterisks ($n = 3$). Scale bar, 50 µm. **J,** Representative immunofluorescence microscopy images of DRG from mice treated with saline or L-OHP stained for Ly6G, H3Cit, and DNA ($n = 3$). Scale bar, 50 µm. (*Continued on the following page.*)

transfected with siRNA oligonucleotides (50 nmol/L) for 6 hours using Lipofectamine 3000 (7.5 μL, L3000008, Thermo Fisher) in 2 mL of OPTI-MEM medium (31985070, Gibco). After 6 hours, the transfection medium was replaced with DMEM culture medium containing 10% FBS and then incubated at 37 °C in 5% CO_2. Transfection was repeated the next day. After 48 hours, whole-cell lysates and cell culture medium were collected.

In vivo multiphoton microscopy

Oxaliplatin-treated and saline-treated mice were i.p. injected with 1% pentobarbital sodium (100 mg/kg, i.p.). To analyze microvascular perfusion, a 0.1 mL bolus of 10 mg/mL FITC-dextran (2,000,000 Da, FD2000S, Sigma-Aldrich) was injected i.v. into the mice. To detect neutrophils, APC-conjugated monoclonal Ly6G antibody (1A8 clone; 3 μg, 17-9668-82, eBioscience) was injected i.v. into mice. To visualize NETs, mice were injected with Sytox Green (10 μL i.v.) 30 minutes before imaging (LSM880 NLO, Zeiss).

IHC

After mice were euthanized, hind paws were severed near the tarsal bones and prepared for histology using routine techniques after decalcification. Briefly, the sections were deparaffinized, rehydrated, and immersed in 3% hydrogen peroxide in methanol to quench endogenous peroxidase activity. Then, the sections were incubated with a blocking buffer for 1 hour. The cross-sections of hind paws were stained with anti-H3Cit (ab5103, Abcam) overnight at 4°C. This was followed by 1-hour incubation with HRP-conjugated goat anti-rabbit IgG (ab207995, Abcam). Staining was visualized by LEICA DM2500 microscopy. For each animal, three fields from cross-sections of the hind paw were visualized under ×20 and ×40 objectives. H3Cit-positive areas were determined.

Flow cytometry

BMDMs were cultured in 6-well plates and stimulated with oxaliplatin (10 μmol/L) for 1 hour. After cultivation, the supernatant was removed, and the cells were washed with PBS. Then, the cells were incubated with dichlorodihydrofluorescein diacetate (DCFH-DA, S0033S, Beyotime Biotechnology) at 10 μmol/L in serum-free medium for 30 minutes at 37°C. After that, the cells were washed with warm PBS and then were removed from plates with cold PBS containing 1% FBS and subjected to flow-cytometric analyses (Miltenyi MACSQuant Analyser 10). For each sample, a total of 10,000 cells were collected, and the ratio of DCFH-DA-positive cells was analyzed through flow cytometry. BMDMs stimulated with rotenone (10 μmol/L, 6 hours) were used as a positive control. The data were analyzed using FlowJo statistical software (v10.62).

Scanning electron microscopy

After isolating mouse neutrophils from bone marrow, neutrophils were stimulated with LPS (1 μg/mL), oxaliplatin (10 μmol/L), or oxaliplatin (10 μmol/L) + LPS (10 ng/mL) and incubated on a 22 × 22 mm cover glass for 4 hours at 37°C in a 5% CO_2 incubator.

Then, the cells were fixed with 2.5% glutaraldehyde for 30 minutes, dehydrated with 25%, 50%, 75%, and 100% ethanol for 10 minutes each time, critical-point dried and then coated with 2 nm platinum (Pt-T4007, DM Material). Because NETs are fragile, each step was done with minimal disturbance of the media to preserve the structures. After dehydration and critical-point drying, the specimens were analyzed under a scanning electron microscope (Helios G4 CX, Thermo Scientific).

Hematoxylin and eosin staining

Colon samples from mice were immersed in 4% PFA for 4 hours and transferred to 70% ethanol. Then, the samples were dehydrated through a serial alcohol gradient and embedded in paraffin wax blocks. Before immunostaining, colon tissue sections were dewaxed in xylene, rehydrated through decreasing concentrations of ethanol, and washed in PBS. Then, the sections were stained with hematoxylin and eosin (C0105S, Beyotime Biotechnology). After staining, sections were dehydrated through increasing concentrations of ethanol and xylene. Finally, images were obtained using a LEICA DM2500 microscope.

Measurement of DRG reactive oxygen species

The level of reactive oxygen species (ROS) in mouse DRG was measured with a kit (S0033S, Beyotime Institute of Biotechnology). Briefly, tissues were finely minced and dissociated with trypsin enzymatic solution (KGY001, Keygen Biotech) by incubation at 37°C for 30 minutes. Then, cells from the mixtures were harvested by centrifugation and washed with PBS twice. Then, the samples were incubated with DCFH-DA (40 μmol/L) in PBS for 40 minutes at room temperature. After that, the samples were centrifuged, washed with PBS twice, and then lysed on ice with lysis buffer (P0013B, Beyotime Biotechnology). Finally, the fluorescence (ex = 488 nm, em = 525 nm) intensity of the supernatant obtained from centrifugation was measured with a multiwell spectrophotometer (Cytation 5, BioTek). The data were normalized to the protein concentrations of the samples.

Statistical analysis

Prism 7.0 (GraphPad) was used to conduct all statistical analyses. Data were statistically evaluated by the Student t test or one-way or two-way ANOVA with the Tukey test. The results are presented as the mean ± standard error of three independent experiments. The results described as significant were based on a criterion of $P < 0.05$.

Data availability statement

All data supporting the findings of this study are available within the article and its Supplementary Data files or from the corresponding author upon reasonable request.

Results

Gut microbiota is critical for oxaliplatin-induced NET formation

Patients who receive oxaliplatin frequently develop OIPN with cold-triggered distal paresthesia; this sensory symptom is sometimes

---

(Continued.) **K,** Representative in vivo multiphoton microscopy images of neutrophils (purple), NETs (red), and vessels (green) in the ears of mice 5 days after the initiation of L-OHP treatment. Neutrophils were localized in ear vessels and in the parenchyma. Blood vessels (green) were labeled by intravenous injection of FITC-dextran (MW = 2,000,000 Da). Neutrophils (purple) were labeled by intravenous injection of APC-conjugated monoclonal Ly6G antibody. NETs (red) were labeled by intravenous injection of Sytox Orange (n = 3). Scale bar, 50 μm. **L,** Mice were administrated 300 μg anti-mouse Ly6G 1 day before the initiation of L-OHP treatment and every 3 days after that until day 14. IgG2α isotype control was administered in the same way. The mechanical pain threshold was tested for 14 days by the von Frey test (n = 6). **M,** WT and Pad4$^{-/-}$ mice were intraperitoneally injected with L-OHP (3 mg/kg) for 5 days. The mechanical pain threshold was tested for 14 days by the von Frey test. **N,** PAD4 inhibitor Cl-amidine (10 mg/kg, i.p.) and MPO inhibitor PF-1355 (50 mg/kg, i.p.) were administered 1 day before the initiation of L-OHP administration once a day until the end of 14 days. The mechanical pain threshold was tested for 14 days by the von Frey test (n = 8). **O,** The concentration of H3Cit in the plasma of mice mentioned in **M** and **N** was evaluated by ELISA on day 14 (n = 6). ***, P < 0.001. Data, mean ± SEM.

paralleled by motor symptoms, including muscle fasciculation and cramps (19, 20). These symptoms are recapitulated in murine models. In our study, mice were exposed to oxaliplatin for 5 consecutive days to induce OIPN. Oxaliplatin-induced mechanical hyperalgesia was assessed by the von Frey test (**Fig. 1A**). Oxaliplatin-treated mice exhibited mechanical touch-induced pain from days 3 to 14 (**Fig. 1B**). In addition, expression of CGRP (an indicator of pain) and c-fos (a marker of activated nociceptive neurons; refs. 21, 22) were increased by oxaliplatin in the spinal cord of mice (Supplementary Fig. S1). These data indicated that we had successfully established an OIPN model in mice.

To determine whether chemotherapy drove NET formation, we assessed the level of H3Cit in the DRG of mice. The primary afferent neurons in DRG serve in the development and maintenance of neuropathic pain (23). Western blot analysis showed an increased amount of H3Cit in the DRG of oxaliplatin-treated mice compared with saline-treated mice (**Fig. 1C**). Furthermore, we found a 2.5-fold increase in the total amount of the neutrophil enzyme MPO in the DRG of mice after oxaliplatin treatment (**Fig. 1D**). Elevated levels of H3Cit, NE, and cfDNA were also found in the plasma from oxaliplatin-treated mice (**Fig. 1E–G**). We also investigated the effect of two other platinum analogues, carboplatin, and cisplatin, as well as paclitaxel and vinblastine, on inducing NET formation. The mechanical hyperalgesia induced by these drugs was assessed by the von Frey test (Supplementary Fig. S2). As shown in **Fig. 1H**, all these chemotherapeutics increased the concentration of cfDNA in the plasma of mice compared with the saline-treated group. The ability of cisplatin to induce NET formation was highest among the chemotherapeutics tested.

Patients who suffer from OIPN show clinical symptoms such as limb paresthesia, weakness, and/or ataxia during chemotherapy. We thus sought to investigate whether NETs emerged in the paws of oxaliplatin-treated mice. IHC staining of cross-sections showed that H3Cit was abundant in the dermis and subcutaneous tissue where sensory neurons were distributed (**Fig. 1I**). Furthermore, confocal microscopy showed that oxaliplatin increased the fluorescence intensity of Ly6G and H3Cit in DRG of mice (**Fig. 1J**). In addition, the colocalization of DNA, Ly6G, and H3cit was abundantly detected in oxaliplatin-treated mice compared with saline-treated mice (**Fig. 1J**). To further confirm that oxaliplatin-induced NET formation, we utilized in vivo multiphoton microscopy of ear vessels, which are easy to investigate. The data indicated that Sytox-labeled NETs abundantly infiltrated the ear vessels at day 5 after oxaliplatin treatment (**Fig. 1K**). Moreover, we found a lower percentage of circulating Ly6G-labeled neutrophils in peripheral blood, which implied that more neutrophils were under NETosis after oxaliplatin treatment (**Fig. 1K**). Next, we depleted neutrophils in mice with an anti-Ly6G, which alleviated mechanical hyperalgesia induced by oxaliplatin (**Fig. 1L**).

PAD4 and MPO are histone-modifying enzymes that are critical for NET formation (24). To further establish the role of NETs in OIPN, we compared wild-type (WT) and $Pad4^{-/-}$ mice, as well as treated mice with the PAD4 inhibitor (Cl-amidine) or the MPO inhibitor (PF-1355) in combination with oxaliplatin. The inhibition of PAD4 or MPO by genetic ablation, Cl-amidine, or PF-1355 reduced the level of H3Cit in plasma and significantly improved oxaliplatin-induced mechanical hyperalgesia (**Fig. 1M–O**). Together, these results suggest that NETs play a critical role in the development of OIPN.

We next investigated the mechanism underlying NET formation during OIPN. A previous study reported that oxaliplatin treatment influenced gut microbiota and destroyed the gut epithelial barrier to permit LPS to enter the circulatory system (9). H&E staining of colon

samples from oxaliplatin- and saline-treated mice showed that intestinal mucosal necrosis, disorderly cell arrangement, and intestinal mucosal thinning occurred in the intestines of mice on the first day they received oxaliplatin and a trend of inflammatory infiltration that became worse on the 3rd and 5th days compared with the saline-treated group (**Fig. 2A**). LPS is a potent NET trigger, and as shown in **Fig. 2B** and **C**, the levels of LPS in the serum and DRG of mice significantly increased after oxaliplatin treatment. Moreover, we collected blood from mice 12 and 24 hours after oxaliplatin administration and then inoculated the plasma into Luria-Bertani (LB) solid medium and LB liquid medium. We found bacterial growth from the blood samples of the oxaliplatin-treated group, with the observation of many bacterial colonies in the LB solid medium and higher turbidity of the LB liquid medium (Supplementary Fig. S3A and S3B). In addition, we found that exposing mice to a cocktail of antibiotics reduced the level of H3Cit and NE in the plasma of oxaliplatin-treated mice and effectively relieved mechanical hyperalgesia (**Fig. 2D–G**). These data implied that gut-derived bacteria played a critical role in oxaliplatin-induced NET formation. We also found that in the process of OIPN, the level of cfDNA in plasma reached a peak at day 7 (Supplementary Fig. S4). The level of LPS in serum increased obviously during the first 3 days and then decreased until 14 days after oxaliplatin treatment (Supplementary Fig. S4). This implied that NETs would be an important factor in the long-term progression of OIPN.

To further confirm that oxaliplatin-induced NET formation, we stimulated neutrophils with oxaliplatin in the presence or absence of LPS and identified NET formation by scanning electron microscopy. As shown in **Fig. 2H**, neither oxaliplatin (10 μmol/L) nor LPS (10 ng/mL) triggered NET formation. In contrast, in the presence of LPS (10 ng/mL), oxaliplatin (10 μmol/L) robustly induced NET formation, like a high concentration of LPS (1 μg/mL), which was used as the positive control. Similarly, immunostaining revealed that in the presence of LPS (10 ng/mL), oxaliplatin (10 μmol/L) stimulated neutrophils to form NETs, which were double stained with H3Cit and MPO antibodies (**Fig. 2I**).

Oxaliplatin induces NET-mediated peripheral neuroinflammation

Macrophage-derived proinflammatory cytokines are attractive targets in the treatment of vincristine-induced neuropathy (VIPN; ref. 15). In our mouse model of OIPN, we also found that oxaliplatin administration markedly increased the levels of IL1β, IL6, and TNFα in plasma and DRG (**Fig. 3A–F**) and increased levels of phospho-NF-κB p65 in the DRG (**Fig. 3G**).

However, the mechanisms underlying macrophage-mediated neuroinflammation in OIPN remain unknown. We hypothesized that NETs played a critical role in these neuroinflammatory responses. A small number of F4/80+ cells were observed in the DRG of saline-treated mice (**Fig. 3H**). Oxaliplatin-induced increased infiltration of macrophages (F4/80+) into the DRG and these cells colocalized with H3Cit. Infiltration of macrophages was decreased in $Pad4^{-/-}$ mice. Consistent with this, the levels of IL1β, IL6, and TNFα were also decreased in the DRG of oxaliplatin-treated $Pad4^{-/-}$ mice (**Fig. 3I–K**). These data indicate that oxaliplatin-induced NETs mediated peripheral neuroinflammation.

NET-mediated NLRP3 activation is required for OIPN via the TLR7/TLR9 pathway

It is widely believed that DNA is the most important component of NETs, but NETs also contain RNA (25). We investigated whether
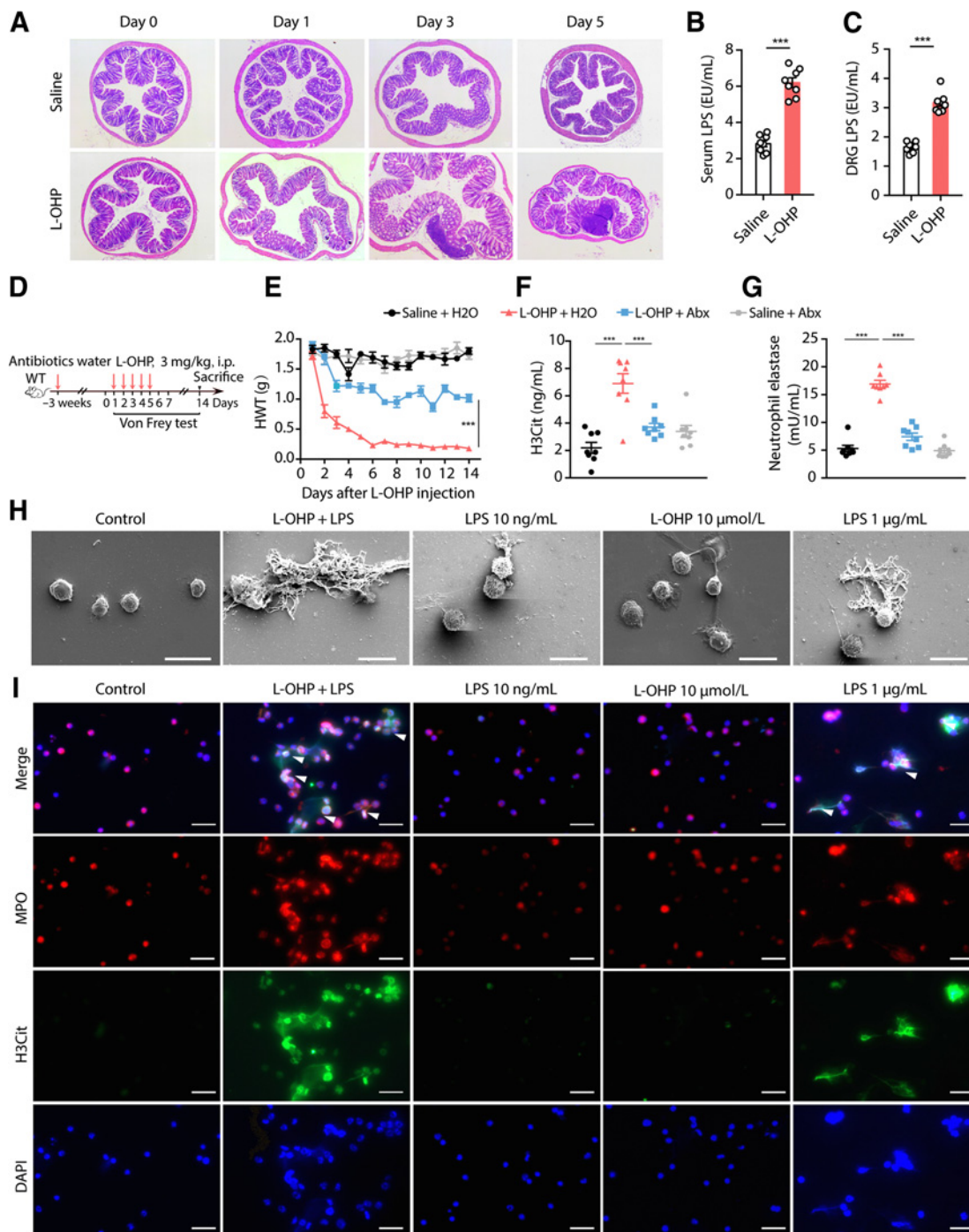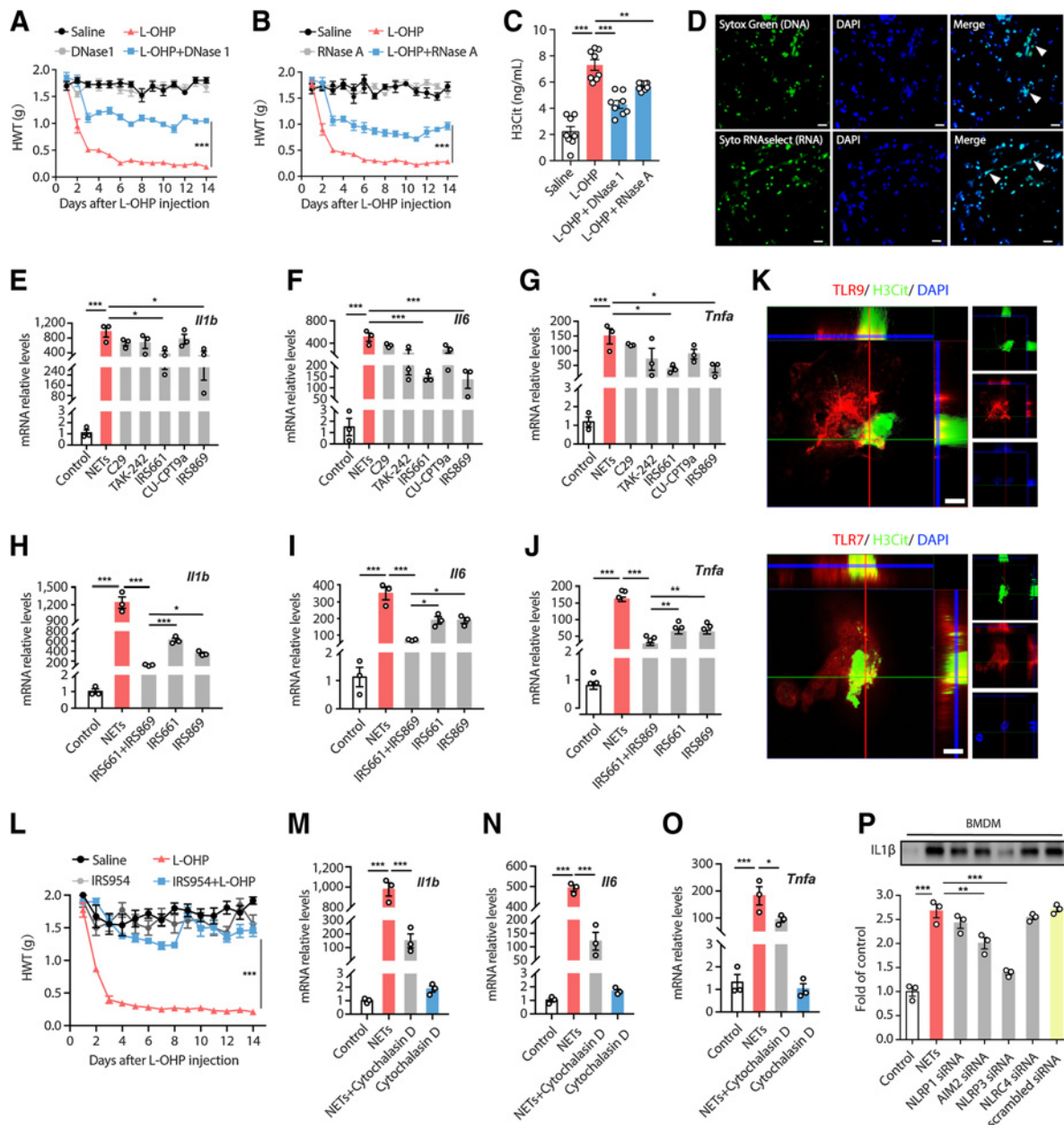
Figure 2.
Chemotherapy induces gut microbe–derived NET formation. Adult male C57BL/6J mice were intraperitoneally injected with L-OHP (3 mg/kg) for 5 days for a total dose of 15 mg/kg. **A,** The degree of intestinal barrier disruption and inflammatory infiltration were evaluated by H&E staining ($n = 3$). Scale bar, 50 μm. **B** and **C,** LPS levels in the serum and DRG of mice were evaluated by Pierce Chromogenic Endotoxin Quant Kit ($n = 8$). **D** and **E,** For gut microbiota eradication, mice were provided drinking water containing 0.5 g/L ampicillin, 0.5 g/L neomycin, 0.5 g/L metronidazole, and 0.25 g/L vancomycin with 3 g/L artificial sweetener Splenda for 3 weeks. Then, the mice were intraperitoneally injected with L-OHP (3 mg/kg) for 5 days. The mechanical pain threshold was tested for 14 days by the von Frey test ($n = 8$). **F** and **G,** The level of H3Cit and NE in plasma was evaluated at day 14 after the initiation of L-OHP treatment using the H3Cit ELISA kit and NETosis Assay, respectively ($n = 8$). **H,** NET formation was examined by scanning electron microscopy following 4 hours of stimulation of neutrophils with LPS (10 ng/mL), L-OHP (10 μmol/L), or LPS (10 ng/mL) + L-OHP (10 μmol/L). Cells treated with LPS (1 μg/mL) were used as a positive control ($n = 3$). Scale bar, 10 μm. **I,** Neutrophils derived from mouse bone marrow were pretreated with LPS (10 ng/mL), L-OHP (10 μmol/L), or LPS (10 ng/mL) + L-OHP (10 μmol/L) for 4 hours, and immunofluorescence staining of NETs was performed: H3Cit (green), MPO (red), and DAPI (blue). The white arrow showed the details of NETs ($n = 3$). Scale bar, 50 μm. ***, $P < 0.001$. Data are shown as mean ± SEM.
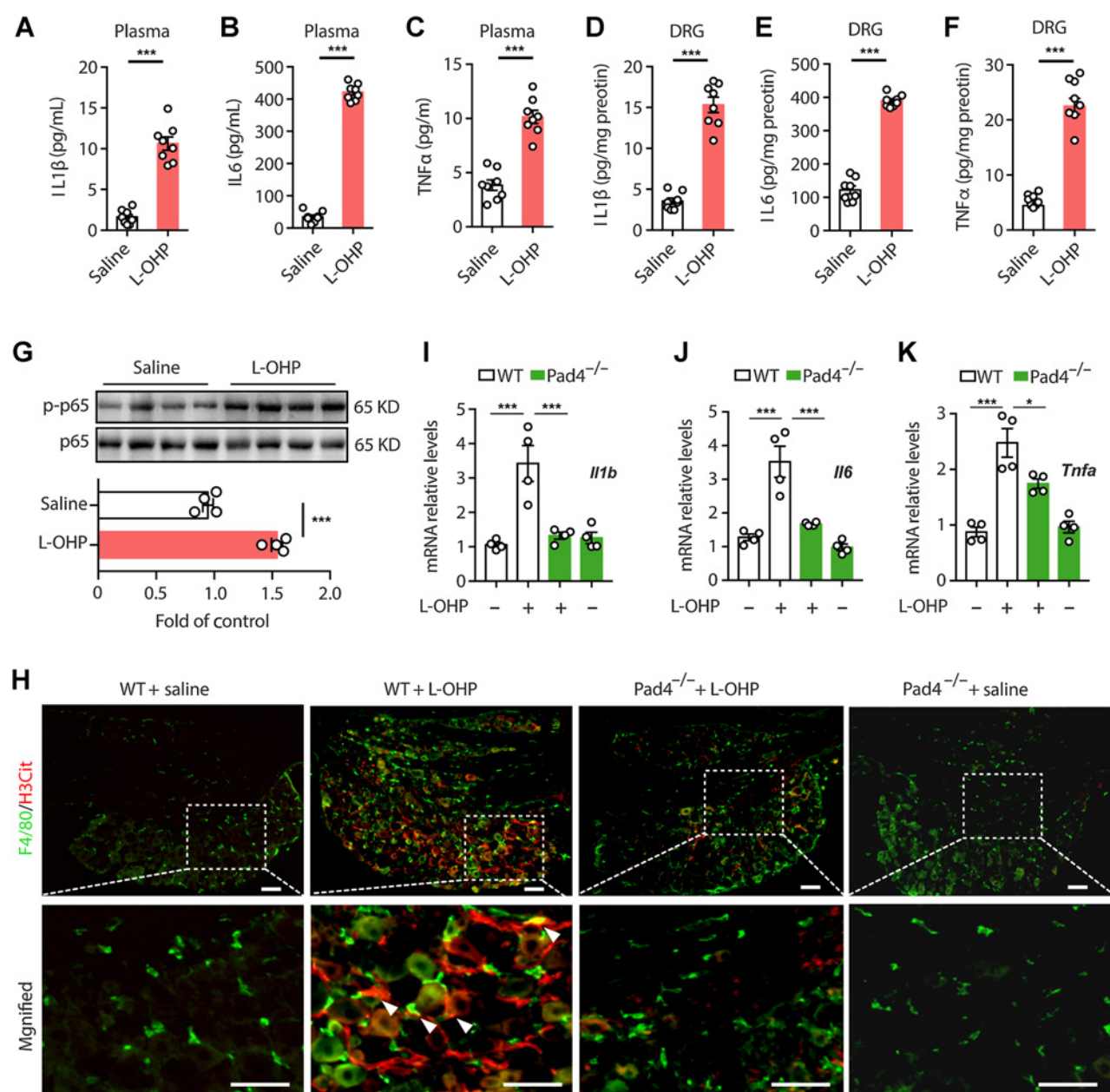
Figure 3.
Oxaliplatin induces NET-mediated proinflammatory cytokine production. **A–F,** Adult male C57BL/6J mice were intraperitoneally injected with L-OHP (3 mg/kg) for 5 days for a total dose of 15 mg/kg. The levels of IL1β, IL6, and TNFα in plasma and DRG were evaluated by ELISA on day 14 after the initiation of L-OHP treatment ($n = 8$). **G,** The level of phospho-NF-κB p65 protein in the DRG was evaluated by western blot on the 14th day after the initiation of L-OHP treatment ($n = 4$). **H,** Representative immunofluorescence microscopy images of DRGs from WT and *Pad4*$^{-/-}$ mice stained with F4/80 (green) and H3Cit (red) on the 14th day after the initiation of L-OHP treatment. The white boxed area shows the details of NETs colocalizing with macrophages (white arrow; $n = 3$). Scale bar, 50 μm. **I–K,** The levels of *Il1b*, *Il6*, and *Tnfa* mRNA in the DRG were evaluated by qPCR at day 14 after the initiation of L-OHP treatment in WT and *Pad4*$^{-/-}$ mice ($n = 4$). ***, $P < 0.001$. Data are shown as mean ± SEM.

the degradation of NETs with DNase 1 or RNase A could alleviate OIPN in mice. The concomitant treatment of mice with DNase 1 or RNase A together with oxaliplatin effectively alleviated neuropathic pain and reduced the level of H3Cit (**Fig. 4A–C**). Moreover, the administration of DNase 1 or RNase A also improved established mechanical hyperalgesia caused by oxaliplatin (Supplementary Fig. S5A–S5C).

We next isolated neutrophils from the mouse bone marrow and incubated them with LPS. Sytox Green–positive extracellular DNA fibers and Syto RNAselect green–positive extracellular RNA were observed (**Fig. 4D**). Excessive NETs can cause severe inflammatory reactions. The stimulation of BMDMs with NETs induced the upregulation of IL1β, IL6, and TNFα (**Fig. 4E**). In addition, our study found that NETs promoted M1-like macrophage polarization

Figure 4.
The TLR7/TLR9 signaling pathway contributes to the activation of the NLRP3 inflammasome induced by NETs. **A** and **B,** Adult male C57BL/6J mice were injected with DNaseI (150 U, i.v.) or RNase A (1 mg/kg, i.v.) from the initiation of L-OHP treatment to the 14th day. The mechanical pain threshold was tested for 14 days by the von Frey test ($n = 8$). **C,** The level of H3Cit in plasma from the mice in **A–B** was evaluated by H3Cit ELISA kit on day 14 after the initiation of L-OHP treatment ($n = 8$). **D,** Neutrophils were incubated in LPS (1 μg/mL) for 4 hours and stained with DNA Sytox Green, RNA Syto RNAselect Green and DAPI (blue). White arrows indicate NETs ($n = 3$). Scale bar, 50 μm. **E–G,** BMDMs were pretreated with a TLR2 inhibitor (C29, 10 μmol/L), TLR4 inhibitor (TAK242, 10 μmol/L), TLR7 inhibitor (IRS661, 1 μmol/L), TLR8 inhibitor (CU-CPT9a, 10 μmol/L), or TLR9 inhibitor (IRS869, 1 μmol/L) for 1 hour and then treated with NETs (500 ng/mL) for 3 hours. The levels of *Il1b*, *Il6*, and *Tnfa* mRNA were measured by qPCR ($n = 3$). **H–J,** BMDMs were pretreated with a TLR7 inhibitor (IRS661, 1 μmol/L) plus a TLR9 inhibitor (IRS869, 1 μmol/L) for 1 hour and then treated with NETs for 3 hours. The levels of *Il1b*, *Il6*, and *Tnfa* mRNA were measured by qPCR ($n = 3$). **K,** Representative immunofluorescence microscopy images of NETs in BMDMs. Neutrophils were incubated with LPS (1 μg/mL) for 4 hours to induce NET formation. Then, BMDMs were treated with NETs for 1 hour and stained with H3Cit (green), TLR7 or TLR9 (red), and DAPI (blue). Each panel represents a section from the stack on the z axis appropriately chosen to visualize the colocalization of H3Cits with TLR7 or TLR9. For each field, two 3D reconstruction sections perpendicular to the plane of the monolayer and parallel to the x or y axis are shown above (x–z section, green line) and to the right (y–z section, red line) of each panel ($n = 3$). Scale bar, 10 μm. **L,** Adult male C57BL/6J mice were administered with inhibitors for TLR7 and TLR9 (IRS954, 10 mg/kg, i.p.) 1 day before the initiation of L-OHP treatment until the end of 14 days. The mechanical pain threshold was tested for 14 days by the von Frey test ($n = 8$). **M–O,** BMDMs were pretreated with cytochalasin D (5 μmol/L) for 1 hour and then treated with NETs for 3 hours. The levels of *Il1b*, *Il6,* and *Tnfa* mRNA were measured by qPCR ($n = 3$). **P,** BMDMs transfected with siRNA targeting the genes encoding NLRP1, AIM2, NLRP3, or NLRC4 were treated with NETs for 3 hours and then treated with oxaliplatin (10 μmol/L) for 1 hour ($n = 3$). Western blot was used to evaluate the levels of IL1β in supernatants. *, $P < 0.05$; **, $P < 0.01$; ***, $P < 0.001$. Data are shown as mean ± SEM.
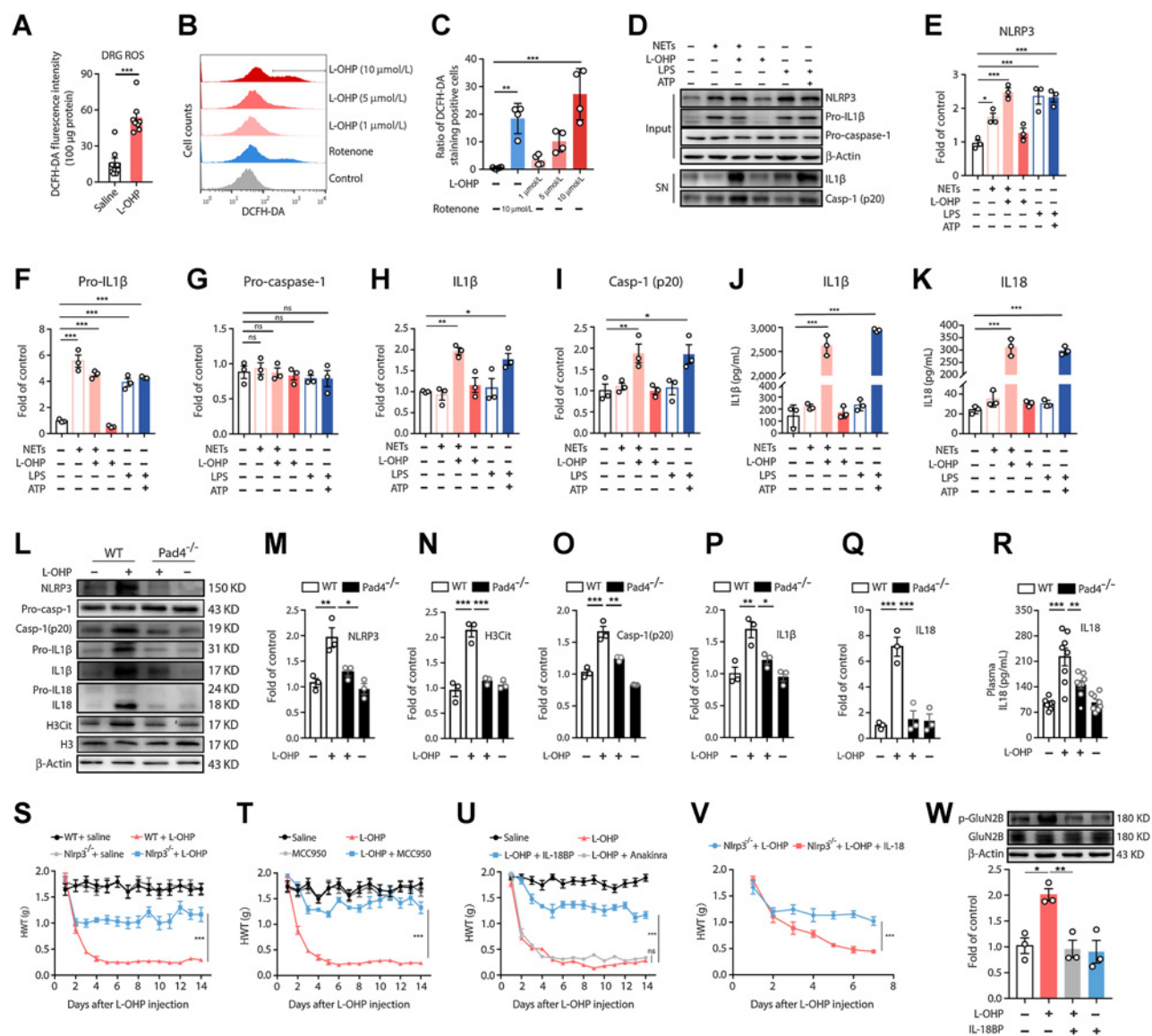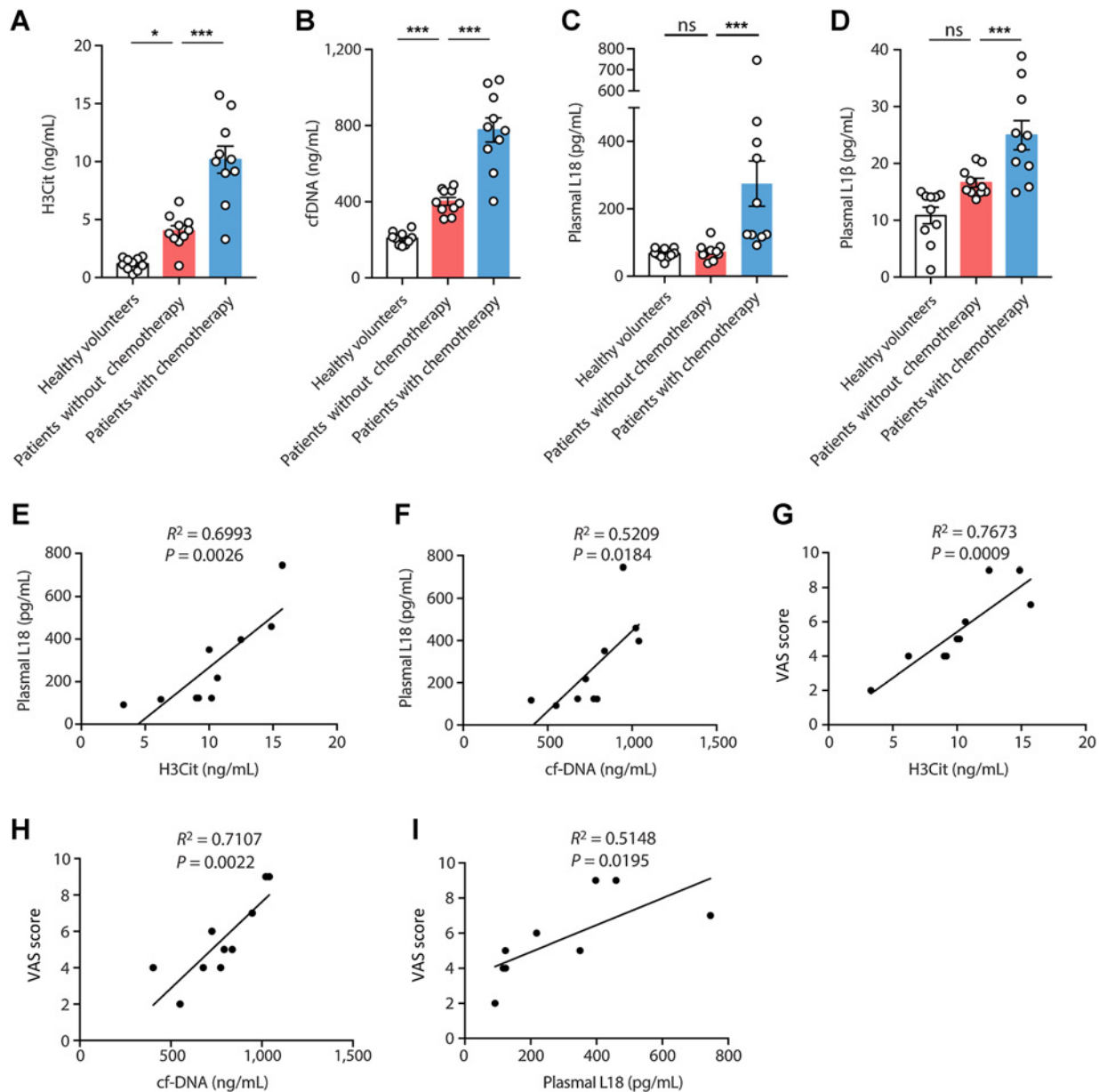
Figure 5.
NLRP3 activation and subsequent IL18 release contribute to oxaliplatin-induced mechanical hyperalgesia. **A,** The level of ROS in the DRG at day 14 after the initiation of L-OHP treatment was assessed by DCFH-DA staining ($n = 8$). **B** and **C,** The level of ROS in BMDMs stimulated with L-OHP (1, 5, or 10 μmol/L) for 1 hour was assessed by calculating the ratio of DCFH-DA–positive cells to 10,000 cells through flow cytometry. BMDMs stimulated with rotenone (10 μmol/L, 6 hours) were used as a positive control ($n = 4$). **D–K,** BMDMs were stimulated with NETs for 3 hours and then stimulated with L-OHP (10 μmol/L) or left unstimulated for 1 hour. LPS (1 μg/mL)-primed BMDMs were treated with ATP (1.5 mmol/L) as a positive control ($n = 3$). Western blot was used to assess the activation of NLRP3 inflammasome–related proteins [NLRP3, Pro-IL1β, Pro-caspase-1, Caspase-1 (p20), IL1β] in BMDMs treated with NETs and/or L-OHP in both culture supernatants [caspase-1 (p20), IL1β] and cell lysates (NLRP3, Pro-IL1β, Pro-caspase-1; **D-I**). IL1β or IL18 in supernatants were analyzed by ELISA (**J** and **K**). **L–Q,** WT and $Pad4^{-/-}$ mice were treated with L-OHP (3 mg/kg) for 5 consecutive days to induce mechanical hyperalgesia. The protein levels of NLRP3, caspase-1 (p20), IL1β, IL18, and H3Cit in the DRG were evaluated on the 14th day by western blot ($n = 3$). **R,** The levels of IL18 in WT and $Pad4^{-/-}$ mice plasma were evaluated by ELISA at day 14 after the initiation of L-OHP treatment ($n = 8$). **S,** WT and $Nlrp3^{-/-}$ mice were treated with L-OHP (3 mg/kg) for 5 consecutive days for a total dose of 15 mg/kg to induce mechanical hyperalgesia. The mechanical pain threshold was tested for 14 days by the von Frey test ($n = 8$). **T,** NLRP3 inhibitor MCC950 (20 mg/kg, i.p.) was administered one day before L-OHP administration until the end of 14 days ($n = 8$). The mechanical pain threshold was tested for 14 days by the von Frey test. **U,** Mice were treated with IL18BP (200 μg/kg, i.p.) or anakinra (2.5 mg/kg, i.p.) 1 day before L-OHP administration. The mechanical pain threshold was tested for 14 days by the von Frey test ($n = 8$). **V,** IL18 (20 ng per mouse, i.p.) was administered one day before L-OHP administration to $Nlrp3^{-/-}$ mice until the end of 7 days. The mechanical pain threshold was measured for 7 days ($n = 6$). **W,** The phosphorylation level of Glu2B in the spinal cord was evaluated on the 14th day after the initiation of L-OHP treatment by western blot ($n = 3$). *, $P < 0.05$; **, $P < 0.01$; ***, $P < 0.001$. Data are shown as mean ± SEM.

with upregulation of the M1 markers IL1β, TNFα, and iNOS and downregulation of the M2 markers Arg1, Fizz1, and CD206 (Supplementary Fig. S6A–S6B).

The DNA component of NETs is known to efficiently induce the dimerization of TLR9 (26, 27). In addition, TLR7 and TLR8 have been shown to be involved in the NET–RNA inflammatory pathway (25). In addition to DNA and RNA, extracellular histones are also key components of NETs (28). Extracellular histones can be recognized by

TLR2 and TLR4 and exert a proinflammatory effect (29). Taken together, TLR2, TLR4, TLR7, TLR8, and TLR9 could potentially be involved in NET-triggered cytokine production. To identify which TLR was critical in this process, we pretreated BMDMs with inhibitors of TLR2, TLR4, TLR7, TLR8, or TLR9 and then stimulated them with NETs. The qPCR data showed that TLR7 and TLR9 inhibitors efficiently inhibited the increased transcription of *Il1b*, *Il6*, and *Tnfa* induced by NETs (**Fig. 4E–G**). Concomitant use of the TLR7 inhibitor

Figure 6.
NETs and IL18 are detected in the plasma of patients after chemotherapy. **A** and **B,** The level of H3Cit and cfDNA, as measured by H3Cit ELISA kit and Quant-iTPico green dsDNA assay, respectively, in plasma from healthy volunteers and cancer patients who had or had not received chemotherapy ($n = 10$). **C** and **D,** The levels of IL18 and IL1β in the same plasma samples used in **A–B** were measured by ELISA ($n = 10$). **E,** Correlations between IL18 and H3Cit were analyzed by linear regression analysis ($R^2 = 0.6993$, $P = 0.0026$). **F,** Correlations between IL18 and cfDNA were analyzed by linear regression analysis ($R^2 = 0.5209$, $P = 0.0184$). **G–I,** Correlations between VAS and H3Cit, cfDNA or IL18 were analyzed by linear regression analysis ($R^2 = 0.7673$, $P = 0.0009$; $R^2 = 0.7107$, $P = 0.0022$; $R^2 = 0.5148$, $P = 0.0195$, respectively). *, $P < 0.05$; ***, $P < 0.001$. Data are shown as mean ± SEM.
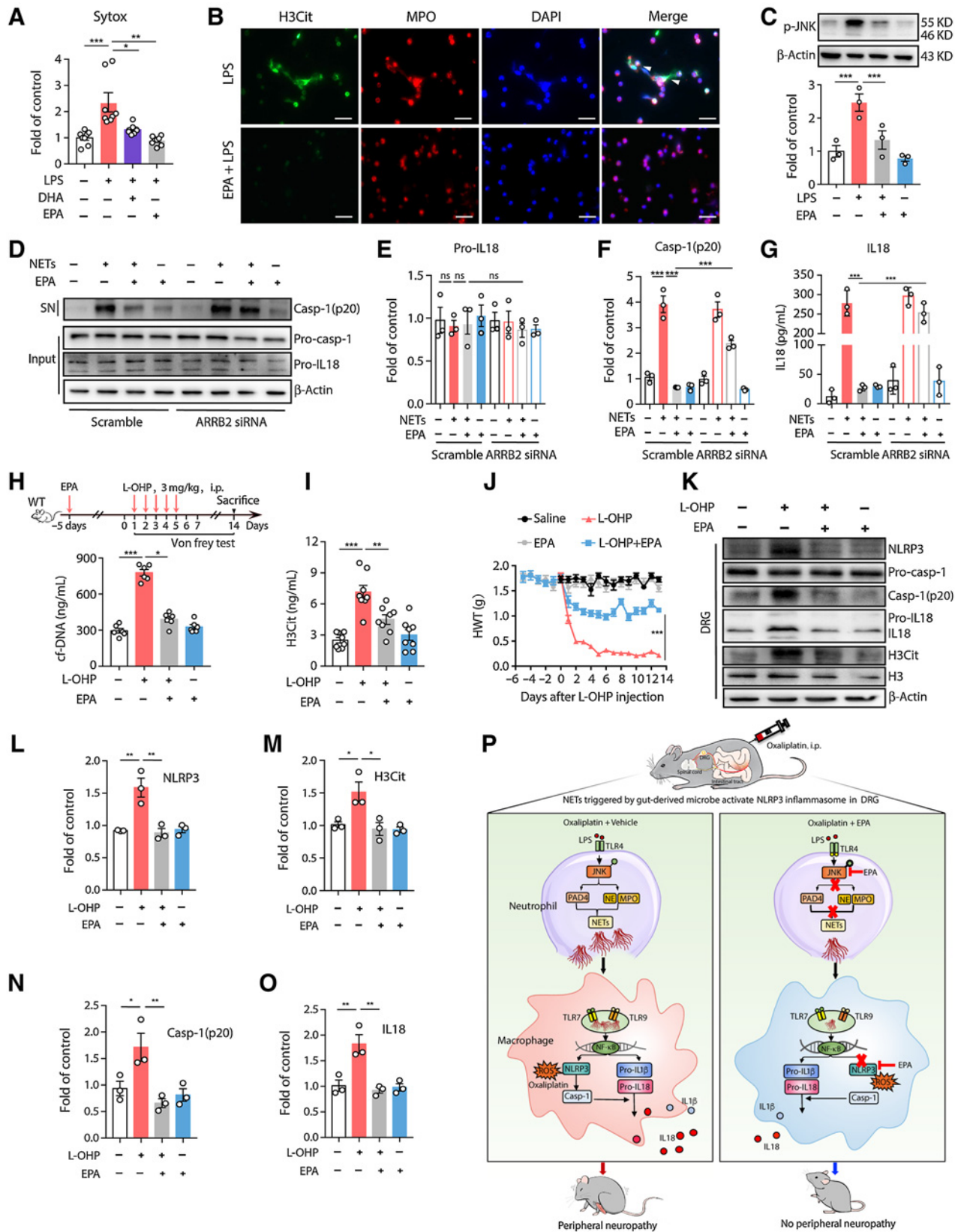
with the TLR9 inhibitor suppressed proinflammatory cytokines most (**Fig. 4H–J**). *Il1b* was inhibited much more than *Il6* and *Tnfa*, with a marked 12-fold decrease in *Il1b* mRNA level, a 5-fold decrease in *Il6* and a 5-fold decrease in *Tnfa* (**Fig. 4H–J**). Immunofluorescence demonstrated H3Cit colocalized with TLR7 and TLR9 in BMDMs (**Fig. 4K**). Similarly, Sytox Orange labeled NETs colocalized with TLR7 and TLR9 receptor in BMDMs (Supplementary Fig. S7). Furthermore, TLR7 and TLR9 inhibitors significantly alleviated OIPN *in vivo* (**Fig. 4L**). Because TLR7 and TLR9 recognize nucleic acids and localize to intracellular compartments, we utilized cytochalasin D to identify whether NETs were endocytosed by macrophages. qPCR data showed that cytochalasin D suppressed the levels of *Il1b*, *Il6*, and *Tnfa* mRNA induced by NETs in BMDMs (**Fig. 4M-O**).

A growing body of evidence supports the notion that IL1β is critical in neuropathic pain. At present, the NLRP1, AIM2, NLRP3, and NLRC4 inflammasomes are reported to be associated with IL1β production (30). Therefore, BMDMs were transfected with siRNA targeting *Nlrp1*, *Aim2*, *Nlrp3*, *Nlrc4*, and *Arrb2* (Supplementary Fig. S8). We found that NLRP3 and AIM2 deficiency, especially NLRP3 deficiency, significantly decreased the level of IL1β induced in BMDMs by NETs (**Fig. 4P**). These results implied that NET-mediated activation of the NLRP3 inflammasome is required for oxaliplatin-induced mechanical hyperalgesia via the TLR7/TLR9 pathway.

NLRP3 activation and subsequent IL18 release contribute to OIPN

Canonical NLRP3 inflammasome activation is a two-step process. First, an NF-κB–activating stimulus induces elevated expression of NLRP3. After this priming, a second signal is required to activate NLRP3 and lead to caspase 1–dependent release of IL1β and IL18. Among the best-characterized activating stimuli are K^+ efflux, Ca^+ flux, lysosomal disruption, and mitochondrial ROS (mtROS; ref. 31). We found that oxaliplatin caused an ROS burst in the DRG of mice (**Fig. 5A**). In addition, DCFH-DA staining showed that oxaliplatin increased the level of ROS in BMDMs (**Fig. 5B** and **C**). Thus, we hypothesized that oxaliplatin-induced ROS could induce the activation of NLRP3. To begin testing this hypothesis, we prepared NETs from LPS-stimulated neutrophils and investigated their effects on BMDMs *in vitro*. Stimulation with either NETs or oxaliplatin produced minor increases in the concentrations of IL1β and IL18 in the supernatants of BMDMs (**Fig. 5D–K**). In contrast, BMDMs released substantial IL1β and IL18 when pretreated with NETs and subsequently stimulated with oxaliplatin. These data indicated that NETs provide an NLRP3 priming signal and oxaliplatin provides an activating signal in IL1β and IL18 production.

Next, we investigated the role of the NLRP3 inflammasome in the development of OIPN. Oxaliplatin-induced upregulation of NLRP3 and subsequent IL1β and IL18 production were reduced in *Pad4$^{-/-}$* mice, as assessed by western blot (**Fig. 5L–Q**). Consistent with this, ELISA data showed that the concentration of IL18 in plasma was significantly lower in *Pad4$^{-/-}$* mice than that in WT mice after treatment of oxaliplatin (**Fig. 5R**). Furthermore, inhibition of NLRP3 by genetic ablation or using the NLRP3 inhibitor MCC950 significantly alleviated OIPN (**Fig. 5S** and **T**).

Activation of the NLRP3 inflammasome drives the release of IL1β and IL18, which are known to sensitize nociceptors. At present, NLRP3-mediated diseases, such as rheumatoid arthritis, are currently managed with biologics targeting IL1β signaling, such as the IL1R antagonist anakinra (31, 32). It has been reported that the IL1R antagonist anakinra could be used to prevent the development of vincristine-induced mechanical hyperalgesia (15). Therefore, we sought to evaluate alleviated mechanical hypersensitivity induced by oxaliplatin, but it did not (**Fig. 5U**). This result suggested that IL18 may play an important role in the development of OIPN in our model. We tested this idea using IL18BP to antagonize the activity of IL18 during OIPN. Symptoms of mechanical hyperalgesia were significantly reversed by IL18BP (**Fig. 5U**). Furthermore, we found that administration of IL18 to *Nlrp3$^{-/-}$* mice elicited mechanical hyperalgesia (**Fig. 5V**). Taken together, these data indicate that NLRP3 activation and subsequent IL18 release contribute to oxaliplatin-induced mechanical hyperalgesia.

It has been reported that IL18 can induce the phosphorylation of Tyr1472 of the GluN2B subunit of N-methyl D-aspartate receptors during bone cancer pain (33). In our study, western blot data showed that the phosphorylation of GluN2B Tyr1472 increased in the spinal cord after oxaliplatin treatment and this increase was significantly suppressed by IL18BP treatment (**Fig. 5W**). IL18 is also recognized as a potent inducer of IFNγ. We found an increased amount of IFNγ in the DRG of oxaliplatin-treated mice, and this increase was suppressed by IL18BP (Supplementary Fig. S9). In addition, treatment with an anti-IFNγ significantly alleviated oxaliplatin-induced mechanical hyperalgesia. Anti-IFNγ increased the pain threshold from 0.3 to 0.8 (Supplementary Fig. S9), whereas IL18BP increased pain threshold from 0.28 to 1.16 (**Fig. 5U**). Our data indicate that IL18 plays a key role upstream of IFNγ in the development of OIPN and suggest that IL18-induced phosphorylation of GluN2B Tyr1472 mediates central sensitization.

Finally, we further validated our data by utilizing plasma from patients with cancer, half of whom had been treated with chemotherapy (Supplementary Tables S1 and S2). As shown in **Fig. 6A–D**, the levels of H3Cit, cfDNA, IL18, and IL1β in plasma from patients with cancer who received chemotherapy were higher than in plasma from

Figure 7.
EPA prevents OIPN by suppressing the formation of NETs and abolishing the activation of NLRP3 inflammasome. **A,** NET formation was quantitatively detected by Sytox Green staining. Bone marrow–derived neutrophils were incubated with LPS (1 μg/mL) for 4 hours. DHA (20 μmol/L) or EPA (20 μmol/L) was added to the medium 1 hour before LPS. Then, the cells were stained with 1 μmol/L Sytox Green for 15 minutes, and fluorescence intensity was captured at an emission peak of 523 nm when excited by a 488 nm argon-ion laser (*n* = 8). **B,** Immunofluorescence staining of NETs was performed: H3Cit (green), MPO (red) and DAPI (blue). The images are representative of three independent experiments. Scale bar, 50 μm. **C,** Bone marrow–derived neutrophils were incubated with LPS (10 μg/mL) for 1 hour, and EPA (20 μmol/L) was added to the medium for 1 hour before LPS treatment. The phosphorylation of JNK was analyzed by western blotting (*n* = 3). **D–G,** BMDMs transfected with *Arrb2*-targeting siRNA were pretreated with EPA (20 μmol/L) for 1 hour before NET stimulation. BMDMs were stimulated with NETs for 3 hours in presence of EPA, and then oxaliplatin (10 μmol/L) was added for 1 hour. Western blot was used to test the activation of NLRP3 inflammasomes–related proteins [Pro-IL18, caspase-1 (p20)] in BMDMs in both culture supernatants (Pro-IL18) and cell lysates [caspase-1 (p20); *n* = 3]. **D–F,** IL18 in supernatants was analyzed by ELISA (*n* = 3). **G. H–O,** EPA (1 g/kg, i.g.) was administered by gavage 5 days before the initiation of L-OHP treatment to the 14th day. The levels of cfDNA and H3Cit in the plasma were evaluated by the Quant-iTPico green dsDNA kit and the H3Cit ELISA kit (*n* = 8; **H–I**). The mechanical pain threshold was tested for 14 days by the von Frey test (*n* = 8; **J**). The protein levels of H3Cit, NLRP3, caspase-1(p20) and IL18 in the DRG were evaluated on the 14th day after the initiation of L-OHP treatment by western blot (*n* = 3; **K–O**). **P,** Schematic illustration indicating that oxaliplatin-induced NETs contribute to the development of OIPN via NLRP3 activation and IL18 release. *, *P* < 0.05; **, *P* < 0.01; ***, *P* < 0.001. Data, mean ± SEM.

patients who did not receive chemotherapy. Spearman correlation analysis showed that there was a positive correlation between IL18 and H3Cit (**Fig. 6E**) and between IL18 and cfDNA (**Fig. 6F**), indicating a positive correlation between NETs formation and neuroinflammation. Furthermore, there was a strong correlation between H3Cit/cfDNA and VAS (**Fig. 6G** and **H**), indicating a positive correlation between NET formation and OIPN. Similarly, we detected a positive correlation between IL18 and VAS (**Fig. 6I**).

EPA prevents OIPN by suppressing the formation of NETs

Omega-3 fatty acids (ω-3 FAs), including EPA and docosahexaenoic acid (DHA), are essential to human health, and deficiencies can lead to chronic diseases (34). Increasing evidence indicates that ω-3 FAs can suppress inflammation and have a beneficial role in a variety of inflammatory human diseases, including diabetes, atherosclerosis, and arthritis (35, 36). ω-3 FAs exert their anti-inflammatory activity via inhibition of inflammasome activation (37). Results from one randomized double-blind placebo-controlled trial showed that ω-3 FAs are protective against paclitaxel-induced peripheral neuropathy in patients with breast cancer (38). However, the mechanisms of the protective effects of ω-3 FAs remain unclear. Here, we assessed whether ω-3 FAs might suppress the formation of NETs besides their ability to inhibit the activation of the NLRP3 inflammasome in OIPN.

First, neutrophils were incubated with LPS to form NETs. Sytox Green staining, indicative of NETs, was significantly decreased when the neutrophils were exposed to PS in the presence of EPA or DHA (**Fig. 7A**). EPA achieved better effects in suppressing NET formation. Immunostaining revealed that EPA inhibited LPS-induced NET formation (**Fig. 7B**). It has been reported that LPS triggers NET formation via the TLR4–JNK pathway (39). Consistent with this idea, we found that EPA decreased LPS-induced phosphorylation of JNK in neutrophils (**Fig. 7C**). We next assessed the effect of EPA on NLRP3 inflammasome activation in BMDMs following priming by NETs. We observed that pretreatment of BMDMs with EPA blocked NET-induced caspase-1 activation and maturation of IL18 in the presence of oxaliplatin (**Fig. 7D–G**). It has been reported that GPR120-ARRB2 is involved in the inhibition of the NLRP3 inflammasome activation by EPA (37). We further investigated the molecular mechanism underlying the inhibitory effect of EPA on NET-induced activation of the NLRP3 inflammasome. We found that downregulation of ARRB2 in BMDMs (Supplementary Fig. S10) abrogated the inhibitory effects of EPA on NLRP3 inflammasome activation (**Fig. 7D–G**). In addition, we evaluated the effect of EPA on BMDMs after stimulation with LPS in the presence or absence of oxaliplatin. We found that EPA suppressed activation of the NLRP3 inflammasome by LPS with or without oxaliplatin (Supplementary Fig. S11A). In fact, EPA inhibited the upregulation of NLRP3 induced by LPS. This indicated that EPA can suppress the first step of NLRP3 inflammasome activation. In addition, we found that EPA blocked LPS-induced caspase-1 activation and maturation of IL18 in the presence of oxaliplatin (Supplementary Fig. S11B). Downregulation of ARRB2 in BMDMs decreased the inhibitory effects of EPA on LPS-induced activation of the NLRP3 inflammasome.

Finally, we investigated whether EPA could prevent OIPN in mice. Mice were treated with EPA for 5 days before oxaliplatin administration. EPA decreased the level of H3Cit and cfDNA in plasma (**Fig. 7H** and **I**) and EPA significantly alleviated mechanical hyperalgesia (**Fig. 7J**), with decreased levels of NLRP3, caspase-1 and IL18 detected in the DRG (**Fig. 7K–O**). Furthermore, we investigated

the effect of EPA on OIPN in neutropenic mice by using anti-Ly6G to deplete neutrophils prior to oxaliplatin treatment. The behavior test data showed that EPA significantly alleviated oxaliplatin-induced mechanical hyperalgesia in neutropenic mice (Supplementary Fig. S11C). Coadministration of EPA and anti-Ly6G significantly alleviated the mechanical hyperalgesia compared with anti-Ly6G alone. Taken together, these results indicated that EPA could prevent OIPN by suppressing the formation of NETs and by abolishing the activation of the NLRP3 inflammasome.

Discussion

Oxaliplatin is a commonly used neurotoxic chemotherapeutic, and the mechanism underlying neurotoxicity is complex. Neuroinflammation has been postulated to contribute to the neurotoxicity induced by oxaliplatin (5). Oxaliplatin administration induces the infiltration of macrophages into DRG and upregulates transcription of the genes encoding IL1β, IL6, and TNFα in DRG neurons (40). Although chemotherapy-associated inflammation is regarded as a key mechanism in the development of OIPN, the pathogenesis underpinning these processes remains elusive.

One study reported that mechanical hyperalgesia was reduced in germ-free mice, indicating a role for the gut microbiota in OIPN (9). LPS, a gram-negative bacterial wall component derived from gut microbiota, enables and augments macrophage secretion of inflammatory cytokines in response to oxaliplatin treatment. Gut microbiota–derived LPS serves as a connection between the gut–neuroimmune axis, forming a complex network influencing the main components involved in the symptoms of OIPN. LPS is a typical bacterial component responsible for inducing the formation of NETs. Although NETs are beneficial for controlling acute infection, excess or dysregulated NETs are associated with many acute inflammation or chronic inflammatory and autoimmune diseases, including COVID-19, sepsis, and vascular diseases (41, 42). The relationship between OIPN and NETs has not been reported. According to previous studies, PAD4 expression in granulocytes is essential for NET formation by promoting histone citrullination. Histone citrullination is thought to facilitate chromatin decondensation and the expulsion of chromosomal DNA in NETs (43). As a result, citrullinated histone H3 is considered a specific biomarker of NETs. Our results showed that oxaliplatin induced increased levels of H3Cit in plasma and DRG. The inhibition of NET formation by *Pad4* gene ablation and PAD4 pharmacologic inhibition ameliorated oxaliplatin-induced mechanical hyperalgesia. In addition, we found that mice treated with oxaliplatin exhibited a disrupted gut epithelial barrier and increased inflammatory infiltration. Treatment with antibiotics reduced the level of NETs in blood and alleviated the mechanical hyperalgesia induced by oxaliplatin.

Next, we sought to investigate whether NETs were critical in oxaliplatin-induced neuroinflammation. We found that *Pad4* gene ablation decreased the infiltration of macrophages and reduced the levels of IL1β, IL6, and TNFα in DRG. These results strongly suggested that NETs could prime macrophage activation and cause proinflammatory cytokine production in OIPN. Activation of NF-κB and release of proinflammatory cytokines often follow TLR stimulation. Some TLRs (TLR1, TLR2, TLR4, TLR5, TLR6, and TLR10) are expressed on the plasma membrane, whereas others (TLR3, TLR7, TLR8, and TLR9) are expressed in the endosome and endoplasmic reticulum (44). NETs are characterized as extracellular DNA fibers, histones, cytoplasmic granule proteins, and RNA.

Considering the components of NETs, we hypothesized that TLR2, TLR4, TLR7, TLR8, and/or TLR9 might be activated during OIPN. Our results showed that NETs promoted macrophage phagocytosis and induced a proinflammatory M1-like macrophage phenotype. Moreover, NETs colocalized with TLR7 and TLR9. These receptors contributed to the upregulation of proinflammatory cytokines induced by NETs. A dual inhibitor of TLR7 and TLR9 significantly alleviated OIPN.

Starobova and colleagues pointed out that IL1β contributed to the development of vincristine-induced neuropathy (15). Thus, we investigated the release of IL1β during OIPN in our model. The maturation and release of IL1β depend on inflammasome activation (30). Four inflammasomes, NLRP1, AIM2, NLRP3, and NLRC4, are critical for the production of IL1β during inflammation (45). Our results showed that NLRP3 and AIM2 deficiency, especially NLRP3 deficiency, significantly reduced the expression of IL1β induced by NETs. NET-triggered NLRP3 inflammasome activation has been previously demonstrated by Liu and colleagues, who reported that NETs could induce an NLRP3-mediated inflammatory response during a diabetic wound (46). NLRP3 inflammasome activation typically requires two steps (47). Our results illustrated that NETs acted as the first signal and that oxaliplatin-induced ROS acted as the second signal in the activation of NLRP3.

Although NLRP3 activation is found in a wide variety of inflammatory diseases, the role of NLRP3 in OIPN is still elusive. We found that oxaliplatin-induced mechanical hyperalgesia was significantly reduced in $Nlrp3^{-/-}$ mice. Direct targeting of NLRP3 by MCC950, a potent and specific NLRP3 inhibitor, significantly alleviated OIPN. In addition to directly targeting NLRP3, the blockade of IL1 signaling is currently used in the treatment of NLRP3-driven autoimmune diseases. Therefore, we investigated anakinra (a recombinant IL1R antagonist) in the treatment of OIPN. However, anakinra failed to suppress OIPN, which implied that IL18 played a very important role in OIPN progression.

It has been reported that IL18-induced phosphorylation of Tyr1472 of the NMDA Receptor GluN2B contributes to bone cancer pain (30). IL18BP is a natural inhibitor of IL18 with high binding affinity. It reduces bioavailability, blocks the effect, and decreases the inflammation caused by IL18 (48, 49). IL18BP enhances morphine and buprenorphine analgesia in neuropathy (50). In our study, we found that IL18BP significantly alleviated OIPN, suggesting that the addition of IL18BP to chemotherapy regimens might be a viable treatment approach for the prevention of OIPN.

Because MCC950 and IL18BP are not available clinically. We wanted to investigate other agents for the treatment of OIPN. A randomized double-blind placebo-controlled trial reported that ω-3 FAs were protective against paclitaxel-induced peripheral neuropathy in patients with breast cancer (38). However, the mechanisms of protective effects remain unclear. Here, we showed that EPA suppressed NET-induced activation of NLRP3 and subsequent IL18 production in vitro and in vivo. We also showed that EPA could inhibit the formation of NETs by inhibiting the LPS–TLR4–JNK pathway. Collectively, our findings demonstrate that EPA provides a new mechanism underlying the treatment of OIPN.

In summary, our study reveals a critical role for NET-mediated NLRP3 activation and IL18 release in the development of OIPN (Fig. 7P). We propose that the occurrence of OIPN is related to the generation of NETs. The DNA and RNA components in NETs prime the activation of NLRP3 via the TLR7/TLR9 pathway. IL18 contributes to oxaliplatin-induced mechanical hyperalgesia. Our data suggest that targeting NLRP3 and IL18 signaling is a potential approach to alleviate OIPN, as is the use of EPA.

Authors' Disclosures

No disclosures were reported.

Authors' Contributions

T. Lin: Data curation, formal analysis, methodology, writing–original draft. **L. Hu:** Data curation, formal analysis. **F. Hu:** Data curation, formal analysis, visualization. **K. Li:** Formal analysis, validation. **C.-Y. Wang:** Data curation. **L.-J. Zong:** Data curation. **Y.-O. Zhao:** Data curation. **X. Zhang:** Resources. **Y. Li:** Resources. **Y. Yang:** Resources. **Y. Wang:** Formal analysis. **C.-Y. Jiang:** Conceptualization, data curation, supervision, funding acquisition, investigation, visualization, methodology, writing–original draft, project administration, writing–review and editing. **X. Wu:** Resources, funding acquisition, project administration. **W.-T. Liu:** Conceptualization, resources, supervision, funding acquisition, investigation, project administration, writing–review and editing.

Note

Supplementary data for this article are available at Cancer Immunology Research Online (http://cancerimmunolres.aacrjournals.org/).

Reference

1. Sereno M, Gutiérrez-Gutiérrez G, Gómez-Raposo C, López-Gómez M, Merino-Salvador M, Tébar FZ, et al. Oxaliplatin induced-neuropathy in digestive tumors. Crit Rev Oncol Hematol 2014;89:166–78.
2. Cersosimo RJ. Oxaliplatin-associated neuropathy: a review. Ann Pharmacother 2005;39:128–35.
3. Kang L, Tian Y, Xu S, Chen H. Oxaliplatin-induced peripheral neuropathy: clinical features, mechanisms, prevention and treatment. J. Neurol 2021;268:3269–82.
4. Cavaletti G, Marmiroli P. Management of oxaliplatin-induced peripheral sensory neuropathy. Cancers 2020;12.
5. Starobova H, Vetter I. Pathophysiology of chemotherapy-induced peripheral neuropathy. Front Mol Neurosci 2017;10:174.
6. Staff NP, Cavaletti G, Islam B, Lustberg M, Psimaras D, Tamburin S. Platinum-induced peripheral neurotoxicity: From pathogenesis to treatment. J Peripher Nerv Syst 2019;24:S26–s39.
7. Lees JG, Makker PG, Tonkin RS, Abdulla M, Park SB, Goldstein D, et al. Immune-mediated processes implicated in chemotherapy-induced peripheral neuropathy. Eur J Cancer 2017;73:22–9.
8. Brandolini L, d'Angelo M, Antonosante A, Allegretti M, Cimini A. Chemokine signaling in chemotherapy-induced neuropathic pain. Int J Mol Sci 2019;20:2904.
9. Shen S, Lim G, You Z, Ding W, Huang P, Ran C, et al. Gut microbiota is critical for the induction of chemotherapy-induced pain. Nat Neurosci 2017;20:1213–6.

10. Sørensen OE, Borregaard N. Neutrophil extracellular traps: the dark side of neutrophils. J Clin Invest 2016;126:1612–20.
11. Papayannopoulos V. Neutrophil extracellular traps in immunity and disease. Nat Rev Immunol 2018;18:134–47.
12. Kumar S, Gupta E, Kaushik S, Jyoti A. Neutrophil extracellular traps: formation and involvement in disease progression. Iran J Allergy Asthma Immunol 2018; 17:208–20.
13. Lee KH, Kronbichler A, Park DD, Park Y, Moon H, Kim H, et al. Neutrophil extracellular traps (NETs) in autoimmune diseases: a comprehensive review. Autoimmun Rev 2017;16:1160–73.
14. Warnatsch A, Ioannou M, Wang Q, Papayannopoulos V. Inflammation: neutrophil extracellular traps license macrophages for cytokine production in atherosclerosis. Science 2015;349:316–20.
15. Starobova H, Monteleone M, Adolphe C, Batoon L, Sandrock CJ, Tay B, et al. Vincristine-induced peripheral neuropathy is driven by canonical NLRP3 activation and IL-1β release. J Exp Med 2021;218:e20201452.
16. Turner PV, Pang DS, Lofgren JL. A review of pain assessment methods in laboratory rodents. Comp Med 2019;69:451–67.
17. Swamydas M, Lionakis MS. Isolation, purification and labeling of mouse bone marrow neutrophils for functional studies and adoptive transfer experiments. J Vis Exp 2013;77:e50586.
18. Najmeh S, Cools-Lartigue J, Giannias B, Spicer J, Ferri LE. Simplified human neutrophil extracellular traps (NETs) isolation and handling. J Vis Exp 2015;98: 52687.
19. Sałat K. Chemotherapy-induced peripheral neuropathy-part 2: focus on the prevention of oxaliplatin-induced neurotoxicity. Pharmacol Rep 2020;72:508–27.
20. Smith EM, Pang H, Cirrincione C, Fleishman S, Paskett ED, Ahles T, et al. Effect of duloxetine on pain, function, and quality of life among patients with chemotherapy-induced painful peripheral neuropathy: a randomized clinical trial. JAMA 2013;309:1359–67.
21. Lee WT, Sohn MK, Park SH, Ahn SK, Lee JE, Park KA. Studies on the changes of c-fos protein in spinal cord and neurotransmitter in dorsal root ganglion of the rat with an experimental peripheral neuropathy. Yonsei Med J 2001;42:30–40.
22. Edvinsson L, Haanes KA, Warfvinge K, Krause DN. CGRP as the target of new migraine therapies: successful translation from bench to clinic. Nat Rev Neurol 2018;14:338–50.
23. Berger AA, Liu Y, Possoit H, Rogers AC, Moore W, Gress K, et al. Dorsal root ganglion (DRG) and chronic pain. Anesth Pain Med 2021;11:e113020.
24. Zhang K, He W, Guo X, Zhang Y, Huang C. [Progress in mechanism of formation of neutrophil extracellular traps: review]. Chin J Cell Molec Immunol 2020;36:561–4.
25. Herster F, Bittner Z, Archer NK, Dickhöfer S, Eisel D, Eigenbrod T, et al. Neutrophil extracellular trap-associated RNA and LL37 enable self-amplifying inflammation in psoriasis. Nat Commun 2020;11:105.
26. Briard B, Place DE, Kanneganti TD. DNA sensing in the innate immune response. Physiology 2020;35:112–24.
27. Silk E, Zhao H, Weng H, Ma D. The role of extracellular histone in organ injury. Cell Death Dis 2017;8:e2812.
28. Allam R, Kumar SV, Darisipudi MN, Anders HJ. Extracellular histones in tissue injury and inflammation. J Mol Med 2014;92:465–72.
29. Daniel C, Leppkes M, Muñoz LE, Schley G, Schett G, Herrmann M. Extracellular DNA traps in inflammation, injury and healing. Nat Rev Nephrol 2019;15:559–75.
30. Man SM, Kanneganti TD. Regulation of inflammasome activation. Immunol Rev 2015;265:6–21.
31. He Y, Hara H, Núñez G. Mechanism and regulation of NLRP3 inflammasome activation. Trends Biochem Sci 2016;41:1012–21.
32. Abbate A, Toldo S, Marchetti C, Kron J, Van Tassell BW, Dinarello CA. Interleukin-1 and the inflammasome as therapeutic targets in cardiovascular disease. Circ Res 2020;126:1260–80.
33. Liu S, Liu YP, Lv Y, Yao JL, Yue DM, Zhang MY, et al. IL-18 contributes to bone cancer pain by regulating glia cells and neuron interaction. J Pain 2018; 19:186–95.
34. Shahidi F, Ambigaipalan P. Omega-3 polyunsaturated fatty acids and their health benefits. Annu Rev Food Sci Technol 2018;9:345–81.
35. Calder PC. Omega-3 fatty acids and inflammatory processes: from molecules to man. Biochem Soc Trans 2017;45:1105–15.
36. Li X, Bi X, Wang S, Zhang Z, Li F, Zhao AZ. Therapeutic potential of ω-3 polyunsaturated fatty acids in human autoimmune diseases. Front Immunol 2019;10:2241.
37. Yan Y, Jiang W, Spinetti T, Tardivel A, Castillo R, Bourquin C, et al. Omega-3 fatty acids prevent inflammation and metabolic disorder through inhibition of NLRP3 inflammasome activation. Immunity 2013;38:1154–63.
38. Ghoreishi Z, Esfahani A, Djazayeri A, Djalali M, Golestan B, Ayromlou H, et al. Omega-3 fatty acids are protective against paclitaxel-induced peripheral neuropathy: a randomized double-blind placebo controlled trial. BMC Cancer 2012;12:355.
39. Khan MA, Farahvash A, Douda DN, Licht JC, Grasemann H, Sweezey N, et al. JNK activation turns on LPS- and gram-negative bacteria-induced NADPH oxidase-dependent suicidal NETosis. Sci Rep 2017;7: 3409.
40. Uhelski ML, Li Y, Fonseca MM, Romero-Snadoval EA, Dougherty PM. Role of innate immunity in chemotherapy-induced peripheral neuropathy. Neurosci Lett 2021;755:135941.
41. Ackermann M, Anders HJ, Bilyy R, Bowlin GL, Daniel C, De Lorenzo R, et al. Patients with COVID-19: in the dark-NETs of neutrophils. Cell Death Differ 2021;28:3125–39.
42. Castanheira FVS, Kubes P. Neutrophils and NETs in modulating acute and chronic inflammation. Blood 2019;133:2178–85.
43. Rohrbach AS, Slade DJ, Thompson PR, Mowen KA. Activation of PAD4 in NET formation. Front Immunol 2012;3:360.
44. Anthoney N, Foldi I, Hidalgo A. Toll and Toll-like receptor signalling in development. Development 2018;145:dev156018.
45. Rathinam VA, Fitzgerald KA. Inflammasome complexes: emerging mechanisms and effector functions. Cell 2016;165:792–800.
46. Liu D, Yang P, Gao M, Yu T, Shi Y, Zhang M, et al. NLRP3 activation induced by neutrophil extracellular traps sustains inflammatory response in the diabetic wound. Clin Sci 2019;133:565–82.
47. Swanson KV, Deng M, Ting JP. The NLRP3 inflammasome: molecular activation and regulation to therapeutics. Nat Rev Immunol 2019;19: 477–89.
48. Zhou T, Damsky W, Weizman OE, McGeary MK, Hartmann KP, Rosen CE, et al. IL-18BP is a secreted immune checkpoint and barrier to IL-18 immunotherapy. Nature 2020;583:609–14.
49. Dinarello CA, Novick D, Kim S, Kaplanski G. Interleukin-18 and IL-18 binding protein. Front Immunol 2013;4:289.
50. Pilat D, Piotrowska A, Rojewska E, Jurga A, S´lusarczyk J, Makuch W, et al. Blockade of IL-18 signaling diminished neuropathic pain and enhanced the efficacy of morphine and buprenorphine. Mol Cell Neurosci 2016;71:114–24.